

The young massive SMC cluster NGC 330 seen by MUSE^{★,★★}

I. Observations and stellar content

J. Bodensteiner¹, H. Sana¹, L. Mahy¹, L. R. Patrick^{2,3}, A. de Koter^{1,4}, S. E. de Mink^{5,4}, C. J. Evans⁶, Y. Götberg⁷,
N. Langer⁸, D. J. Lennon², F. R. N. Schneider⁹, and F. Tramper¹⁰

¹ Instituut voor Sterrenkunde, KU Leuven, Celestijnenlaan 200D, 3001 Leuven, Belgium
e-mail: julia.bodensteiner@kuleuven.be

² Instituto de Astrofísica de Canarias, 38205 La Laguna, Tenerife, Spain

³ Universidad de La Laguna, Dpto. Astrofísica, 38206 La Laguna, Tenerife, Spain

⁴ Astronomical Institute Anton Pannekoek, Amsterdam University, Science Park 904, 1098 Amsterdam, The Netherlands

⁵ Center for Astrophysics, Harvard & Smithsonian, 60 Garden Street, Cambridge, MA 02138, USA

⁶ UK Astronomy Technology Centre, Royal Observatory, Blackford Hill, Edinburgh EH9 3HJ, UK

⁷ The observatories of the Carnegie institution for science, 813 Santa Barbara St., Pasadena, CA 91101, USA

⁸ Argelander-Institut für Astronomie, Universität Bonn, Auf dem Hügel 71, 53121 Bonn, Germany

⁹ Heidelberger Institut für Theoretische Studien, Schloss-Wolfsbrunnengasse 35, 69118 Heidelberg, Germany

¹⁰ Institute for Astronomy, Astrophysics, Space Applications & Remote Sensing, National Observatory of Athens, P. Penteli 15236, Athens, Greece

Received 19 September 2019 / Accepted 6 November 2019

ABSTRACT

Context. A majority of massive stars are part of binary systems, a large fraction of which will inevitably interact during their lives. Binary-interaction products (BiPs), that is, stars affected by such interaction, are expected to be commonly present in stellar populations. BiPs are thus a crucial ingredient in the understanding of stellar evolution.

Aims. We aim to identify and characterize a statistically significant sample of BiPs by studying clusters of 10–40 Myr, an age at which binary population models predict the abundance of BiPs to be highest. One example of such a cluster is NGC 330 in the Small Magellanic Cloud.

Methods. Using MUSE WFM-AO observations of NGC 330, we resolved the dense cluster core for the first time and were able to extract spectra of its entire massive star population. We developed an automated spectral classification scheme based on the equivalent widths of spectral lines in the red part of the spectrum.

Results. We characterize the massive star content of the core of NGC 330, which contains more than 200 B stars, 2 O stars, 6 A-type supergiants, and 11 red supergiants. We find a lower limit on the Be star fraction of $32 \pm 3\%$ in the whole sample. It increases to at least $46 \pm 10\%$ when we only consider stars brighter than $V = 17$ mag. We estimate an age of the cluster core between 35 and 40 Myr and a total cluster mass of $88^{+17}_{-18} \times 10^3 M_{\odot}$.

Conclusions. We find that the population in the cluster core is different than the population in the outskirts: while the stellar content in the core appears to be older than the stars in the outskirts, the Be star fraction and the observed binary fraction are significantly higher. Furthermore, we detect several BiP candidates that will be subject of future studies.

Key words. stars: massive – stars: emission-line, Be – binaries: spectroscopic – blue stragglers – Magellanic Clouds – open clusters and associations: individual: NGC 330

1. Introduction

Massive stars, that is, stars with birth masses higher than $8 M_{\odot}$, have played a major role throughout the history of the Universe (Jamet et al. 2004; Bresolin et al. 2008; Aoki et al. 2014). Despite their low numbers and short lifetimes, they have a strong effect on their environment. They heat, shape, and enrich their surroundings with their high temperatures and luminosities, strong stellar winds, and final explosions (Bromm et al. 2009; de Rossi et al. 2010). Massive stars can evolve following

a diversity of evolutionary channels. Which channel a star follows depends most significantly on its initial mass, metallicity, rotation, and multiplicity.

Recent observations have shown that a vast majority of massive stars do not evolve as single stars (see, e.g., Sana et al. 2012; Kobulnicky et al. 2014; Dunstall et al. 2015). In contrast, they reside in binary systems and will at some point in their lives interact with a nearby companion (Sana et al. 2012). In addition to stable mass transfer in terms of Roche-lobe overflow, more dramatic interactions such as common-envelope evolution and stellar mergers are possible (Taam & Sandquist 2000; de Mink et al. 2014; Kochanek et al. 2019). In any of these cases, the stellar mass and angular momentum change significantly, which will drastically alter the evolutionary path of the two stars (Podsiadlowski et al. 1992; Vanbeveren & De Loore 1994).

* Full Table D.1 is only available at the CDS via anonymous ftp to cdsarc.u-strasbg.fr (130.79.128.5) or via <http://cdsarc.u-strasbg.fr/viz-bin/cat/J/A+A/634/A51>

** Based on observations collected at the ESO Paranal observatory under ESO program 60.A-9183(A).

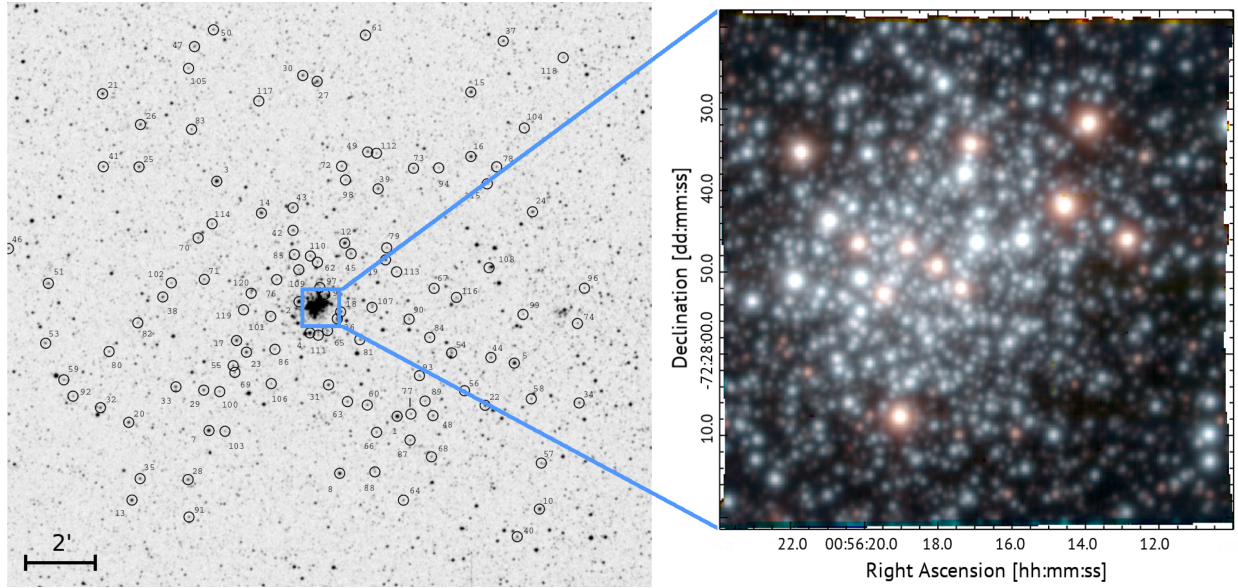


Fig. 1. *Left:* finding chart from Evans et al. (2006), where stars that were studied are marked with black circles and the FoV of MUSE is indicated in blue. *Right:* true-color image created by convolving the MUSE data with a *B*, *V*, and *I* filter. At the distance of NGC 330, the size of the FoV of $1' \times 1'$ corresponds to $\sim 20 \times 20$ pc.

Understanding the detailed evolution of massive stars while taking the effect of multiplicity into account remains one of the greatest challenges in modern astrophysics (Langer 2012).

One possible line of investigation for exploring the effect of multiplicity on the evolution of massive stars is to study stars after they have interacted, that is, binary-interaction products (BiPs). The outcome of the interaction process, which defines the physical properties of such BiPs, indeed remains ill constrained. Characterizing the physical properties of BiPs, however, is crucial for assessing their current effect on their surroundings and predict their future evolution. This in turn defines the nature and quantity of key end-of-life products, such as supernova types and the strength of supernova kicks, the nature and multiplicity properties of compact objects, and ultimately, those of gravitational wave events.

The BiPs can be identified through various stellar properties, none of which, unfortunately, ensures an unambiguous identification. Through the transfer of angular momentum, mass gainers or merger products may be expected to be rotating rapidly (de Mink et al. 2013; Mahy et al. 2020). The transfer of mass may lead to abnormal chemical abundances on the stellar surface (de Mink et al. 2007; Langer 2012). The supernova explosion of the more massive star can disrupt the system, turning the secondary into a so-called runaway star, which is a star that moves away from its birth place with a high space velocity (Gies & Bolton 1986; Blaauw 1993; Hoogerwerf et al. 2001). If the system remains bound, an excess in UV or hard X-ray flux may indicate the presence of a compact companion, like in the case of subdwarf companions (see, e.g., Gies et al. 1998; Wang et al. 2017, 2018) and X-ray binaries (Verbunt 1993; Reig 2011). In star clusters, mass-gainers and mergers are expected to appear younger than their sibling stars, that is, they are bluer and hotter than the main-sequence turnoff and are massive analogs to the blue stragglers that are found in globular clusters (see, e.g., Sandage 1953; Shara et al. 1997; Ferraro et al. 1997; Schneider et al. 2015). Recently, their cooler equivalent was proposed by Britavskiy et al. (2019) and Beasor et al. (2019): so-called red stragglers, which are red supergiants (RSGs) that are more massive and luminous than expected from single-star evolution.

Next to the study of the well-known post-mass-transfer Algol systems, searches for BiPs were conducted in several manners in the past: numerous photometric studies found blue stragglers in all types of star clusters (see, e.g., Ferraro et al. 1997; Ahumada & Lapasset 2007; Gosnell et al. 2014). Schneider et al. (2014) reported indications for BiP signatures in the mass function of young clusters, while Ramírez-Agudelo et al. (2013, 2015) found a significant proportion of fast rotators in the presumably single O-type stars in 30 Dor. The relative fraction of these were compatible with population synthesis predictions of BiPs (de Mink et al. 2013, 2014). The search for BiPs was extended to magnetic stars through the Binary and Magnetism survey (BinaMIcS, Alecian et al. 2015; Schneider et al. 2016). Bodensteiner et al. (2018) proposed to use infrared nebulae around massive stars that may have formed in previous binary interactions as general tracers for BiPs.

Population synthesis simulations show that the relative contributions of BiPs to the lower mass content of the cluster vary as a function of age and peak between 8 and 40 Myr, assuming a single starburst (Schneider et al. 2015). While much effort has been invested in spectroscopically characterizing the massive star content of young massive star clusters (see, e.g., Evans et al. 2011; Sana & Evans 2011; Clark et al. 2014; Ramírez-Tannus et al. 2018, and references therein), these slightly older populations have been somewhat overlooked.

Here we aim to investigate the massive star population of the young open star cluster NGC 330. This cluster is situated in the Small Magellanic Cloud (SMC) at a distance of 60 ± 1 kpc (Harries et al. 2003; Hilditch et al. 2005; Deb & Singh 2010). Age estimates of NGC 330 vary between 26 and 45 Myr, which places it in the age range of interest for our purposes (Sirianni et al. 2002; Martayan et al. 2007b; Milone et al. 2018; Patrick et al. 2020). The estimated photometric mass of NGC 330 ranges between $M_{\text{phot}} \approx 3.6 \times 10^4 M_{\odot}$ (McLaughlin & van der Marel 2005) and $M_{\text{phot}} \approx 3.8 \times 10^4 M_{\odot}$ (Mackey & Gilmore 2002), which agrees well with a recent estimate of the dynamical mass $M_{\text{dyn}} = 15.8^{+7.6}_{-5.1} \times 10^4 M_{\odot}$ (Patrick et al. 2020).

Several spectroscopic studies of the brightest stars in NGC 330 were conducted in the past, reporting a high Be star fraction

of about 50% or higher (Feast 1972; Grebel et al. 1992, 1996; Lennon et al. 1993; Mazzali et al. 1996; Keller & Bessell 1998; Keller et al. 1999). Based on these findings, Maeder et al. (1999) concluded that the Be star fraction in the SMC is higher than that in the Large Magellanic Cloud and in the Milky Way. A high Be star fraction in SMC clusters (excluding NGC 330) was confirmed by Martayan et al. (2007b). Around 150 OB stars situated in the outskirts of NGC 330 were studied spectroscopically (Evans et al. 2006). Additionally, the cluster was recently investigated by Milone et al. (2018) using *Hubble* Space Telescope (HST) photometry. The dense cluster core, which contains more than 100 massive stars, could not be resolved with existing spectroscopic instrumentation. It is, however, the region where except for runaways, many of the massive BiPs are expected as a result of mass segregation, whether primordial (Sirianni et al. 2002) or as a result of cluster dynamics (Portegies Zwart et al. 2010).

In this first paper of a series, we report on a spectroscopic study of the core of NGC 330 with the Multi-Unit Spectroscopic Explorer (MUSE) mounted at Unit 4 of the Very Large Telescope (VLT/UT4, Bacon et al. 2010). Its capabilities have recently been enhanced with adaptive optics (AO), and it is now possible to efficiently obtain spectroscopy of individual stars in the dense cluster core. This first paper focuses on the method for extracting spectra and on the stellar content of the cluster. Future papers will address multiplicity and physical properties of the stars in the cluster. In Sect. 2 we summarize the observations and the data reduction. Section 3 describes the automatic routine we developed to extract spectra of stars brighter than $V = 18.5$ mag. In Sect. 4 we explain how spectral types can be automatically determined based on the equivalent widths of certain spectral lines between 4600 Å and 9300 Å. We present the stellar content of the cluster core in Sect. 5 and compare it to previous photometric and spectroscopic studies of the cluster. Section 6 gives a summary and conclusions.

2. Observations and data reduction

2.1. Observations with MUSE-WFM-AO

NGC 330 was observed with MUSE on 19 November 2018 at Yepun, one of the four Unit Telescopes of the VLT in Paranal, Chile. MUSE is an integral-field spectrograph comprising 24 individual spectrographs.

In wide-field mode (WFM), the 24 individual spectrographs sample a field of view (FoV) of $1' \times 1'$ with a spatial sampling of $0.2''$ in both directions. The seeing during the observations varied between $0.4''$ and $0.7''$. With the new AO, the MUSE-WFM observations are supported by ground-layer adaptive optics (GLAO) consisting of a deformable secondary mirror, four sodium laser guide stars, and the Ground Atmospheric Layer Adaptive OptiCs for Spectroscopic Imaging (GALACSI) module. The observations were carried out in the extended wavelength mode covering a broad optical range (i.e., 4600 Å–9300 Å). When the observations are supported by AO, the region between 5780 and 5990 Å is blocked by a notch filter in order to avoid light contamination by the sodium lasers of the AO system. The spectral resolving power ranges from 2000 at 4600 Å to 4000 at 9300 Å.

Five dither positions (DPs) of 540 seconds each were obtained with a relative spatial offset of about $0.7''$. The instrument derotator was offset by 90° after each DP so that the light of each star was dispersed by multiple spectrographs. Directly after the observation of NGC 330, an offset sky observation for sky subtraction was taken (see Sect. 2.3). A comparison between the finding chart

of Evans et al. (2006) and a true-color image showing the spatial coverage of the MUSE observations is shown in Fig. 1.

2.2. Data reduction

The MUSE data were reduced with the standard ESO MUSE pipeline v2.6¹. The calibrations for each individual IFU included bias and dark subtraction, flat fielding, and wavelength and illumination correction. After recombining the data from each IFU to the merged data cube, a telluric correction and a flux calibration was performed with the help of a standard star observation. Furthermore, the sky was subtracted in different manners to obtain the best possible result (see Sect. 2.3). The output of the data reduction is a so-called 3D data cube containing two spatial and one spectral direction of dimensions $321 \times 320 \times 3701$. This can either be thought of as 3701 monochromatic images or as about 10^5 individual spectra.

In previous versions of the ESO MUSE pipeline (up to v2.4.1), large-scale (i.e., about 50 \AA wide) wiggles dominated the blue part of the spectrum when the MUSE-WFM-AO setup was used. While this problem was fixed in the data extension itself in v2.6, it still occurs in the variance of the reduced MUSE data.

2.3. Sky subtraction

Different methods can be used to subtract the sky in the ESO MUSE pipeline. As described in Sect. 2.1, an offset sky exposure was taken at the end of the observational sequence. It is supposed to be centered on an effectively empty sky region, but close to the target region. This facilitates the detection of a dark patch of sky that is not contaminated by stars in order to determine an average sky spectrum. While this procedure works well for isolated objects like galaxies, in the case of NGC 330, which is situated in a dense region of the SMC, it is difficult to find a nearby empty region. In this case, the sky observation is only $3'$ away of the science observation and is equally crowded by SMC stars so that the benefits of the sky observation are limited.

Extensive testing showed that the remaining sky residuals are smaller when the sky background is estimated from the science observations themselves. The MUSE pipeline offers the required framework in which a fraction of the darkest pixels in the science observation is used to estimate an average sky spectrum. This is then subtracted from the science data. The advantage of this method in comparison to using the sky cube is that the average sky spectrum is taken at exactly the same time and thus under the exact same weather and atmosphere conditions.

A comparison between the two different sky subtraction methods for a bright star (top panel) and a faint star (bottom panel) is shown in Fig. 2. The figure illustrates that (1) sky subtraction is an important task in the data reduction, and (2) that the residual sky emission lines are smaller when the data cube is used instead of the sky cube (see, e.g., at $\lambda\lambda 6300, 6365 \text{ \AA}$).

3. Extraction of stellar spectra

3.1. Target input catalog

To extract spectra from the MUSE data, we required an input list of stars including stellar positions and brightnesses. We adopted a magnitude cut at $V = 18.5$ mag, which approximately corresponds to $6 M_\odot$ at the SMC distance and extinction. This results in a signal-to-noise (S/N) of about 80, which is high enough for our further analysis.

¹ <https://www.eso.org/sci/software/pipelines/muse/>

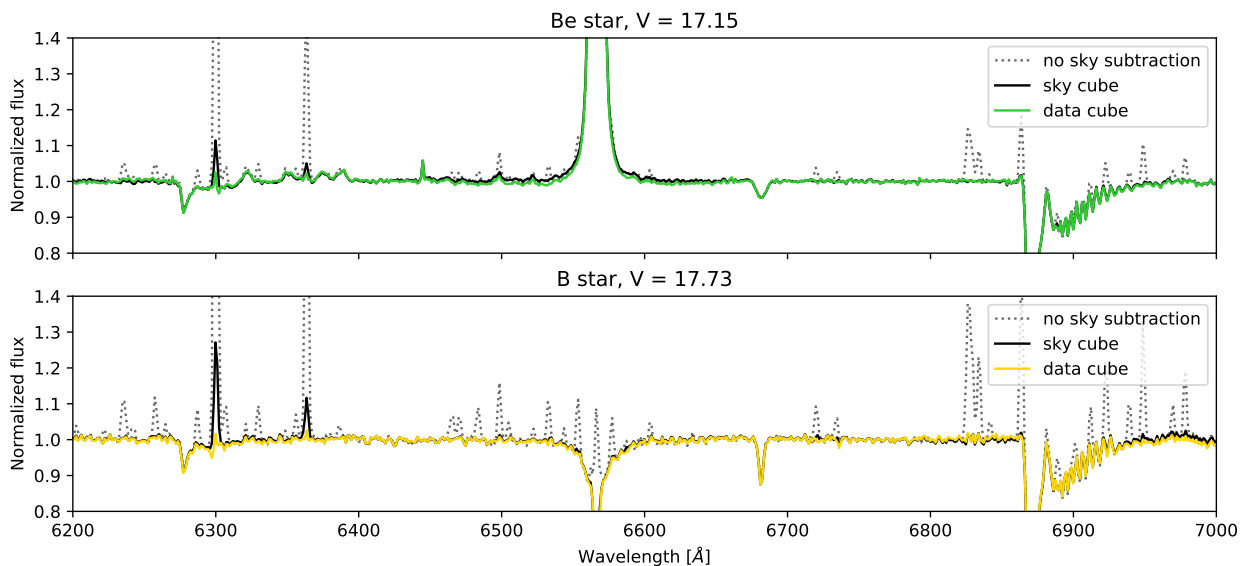


Fig. 2. Comparison of the sky-subtraction methods for two example stars (marked in Fig. 5 with the corresponding colors). The *top panel* gives the spectra of an example bright star (star 152, a Be star with $V = 17.15$ mag), and the *bottom panel* gives those of a fainter star (star 111, a B star with $V = 17.51$ mag). We show for both stars the original spectrum without any sky subtraction (no sky subtraction), the spectrum with the sky subtraction deduced from the dedicated sky cube (sky cube), and the spectrum with the sky subtraction determined in the science data cube (data cube). The spectra are not corrected for telluric lines (see, e.g., the region between 6850 and 7000 Å).

Accurate stellar positions can be directly estimated in the MUSE data. They are, however, preferably determined from an instrument of higher spatial resolution such as the HST, which provides an approximately ten times better spatial resolution. The core of NGC 330 was observed with WFPC2 and the $F555W$ filter (approximately corresponding to the V band) in 1999, and with WFPC3 and the $F336W$ filter (approximately corresponding to the U band) in 2015. Unfortunately, the $F555W$ filter image does not cover the full MUSE FoV (see Fig. 3). The $F336W$ data cover the whole FoV, but the filter is outside the wavelength range covered by MUSE. For both images, an automatically created source list based on DAOPhot is available in the HST archive². The brightest stars (i.e., stars brighter than $V < 15$ mag) are saturated in the HST images and are therefore missing in the input list.

Figure 3 shows that the coordinate systems in both HST input catalogs are not aligned with the MUSE world coordinate system (WCS). We therefore first aligned the two HST catalogs with each other, and in a subsequent step aligned them with the MUSE WCS. For this, we selected a handful of isolated stars in the MUSE image, determined their positions by fitting a point-spread function (PSF), and then computed the coordinate transformation between these known sources in MUSE and in the aligned HST catalogs. The coordinate transformation from the HST coordinate system (x', y') into the MUSE coordinate system (x, y) is given by

$$x = +x' \cdot \cos(\theta) + y' \cdot \sin(\theta) + \Delta x \quad (1)$$

$$y = -x' \cdot \sin(\theta) + y' \cdot \cos(\theta) + \Delta y. \quad (2)$$

The best-fit values derived for the coordinate transformation are $\Delta x = (1.79 \pm 0.36)$ px, $\Delta y = (1.06 \pm 0.43)$ px, and $\theta = (-0.05 \pm 0.10)^\circ$. This transformation was applied to all HST sources.

To obtain a complete target list containing V magnitudes of all stars, we combined the $F336W$ and the $F555W$ list. We used stars that appear in both lists and are brighter than 19.5 in $F555W$

to compute a correlation between $F555W$ magnitudes and $F336W$ magnitudes. This allowed us to approximately convert $F336W$ magnitudes into $F555W$ magnitudes for stars that are not covered by the $F555W$ data (see Figs. 3 and 4). This conversion is only accurate for early-type main-sequence stars, for which the U -band filter covers the Rayleigh-Jeans tail of the spectrum. It does not hold for stars that are evolved off the main sequence (MS), for instance, for RSGs and blue supergiants (BSGs). As mentioned above, given the brightness of these stars, they are saturated in the HST images. For the same reason, on the other hand, they have previously been studied (see, e.g., Arp 1959; Robertson 1974; Grebel et al. 1996). We therefore adopted their V -band magnitudes from Robertson (1974) when available (see Table 2).

The final target list was constructed by taking all sources that are within the MUSE field of view and brighter than $V = 18.5$ mag. Seven stars that are clearly brighter than $V = 18.5$ mag are missing in both HST input lists. This is probably due to problems in the automated source-finding routines. These seven stars were added manually before we constructed the final target list, which contains 278 stars.

3.2. Source extraction

The high source density especially in the center of the image and the associated spatial overlap of sources complicates extracting stellar spectra. Given the format of the reduced MUSE data (i.e., a 3D data cube with two spatial and one spectral dimension), obtaining a spectrum of a source is equivalent to measuring its brightness in each wavelength image (referred to as a slice in the following). We avoided simple aperture photometry (i.e., adding up the flux in a given aperture around each star's position) in each slice because the field is so crowded.

We developed our own spectral extraction routine that employs PSF fitting. The routine is mainly based on the PYTHON package PHOTUTILS (Bradley et al. 2019), a translation of DAOPhot (Stetson 1987) into PYTHON, which provides a framework for PSF fitting in crowded fields. We used the input

² <https://archive.stsci.edu/hst/>

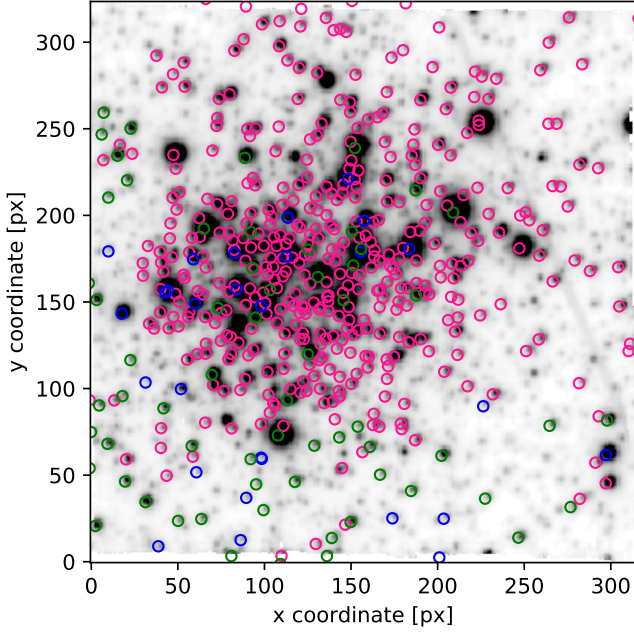


Fig. 3. Source positions from the HST overlaid over an integrated-light image extracted from the MUSE cube. Stars with only $F336W$ magnitudes are marked in pink, and stars with only $F555W$ magnitudes are marked in blue. Stars that appear in both lists and are brighter than 19.5 in $F555W$ are marked in green. They are used to determine a correlation between the two magnitudes (see Fig. 4). The two HST source catalogs need to be aligned with respect to the MUSE coordinate system by shifting them by $\Delta x = (1.79 \pm 0.36)$ px and $\Delta y = (1.06 \pm 0.43)$ px, and rotating them by $\theta = (-0.05 \pm 0.10)^\circ$.

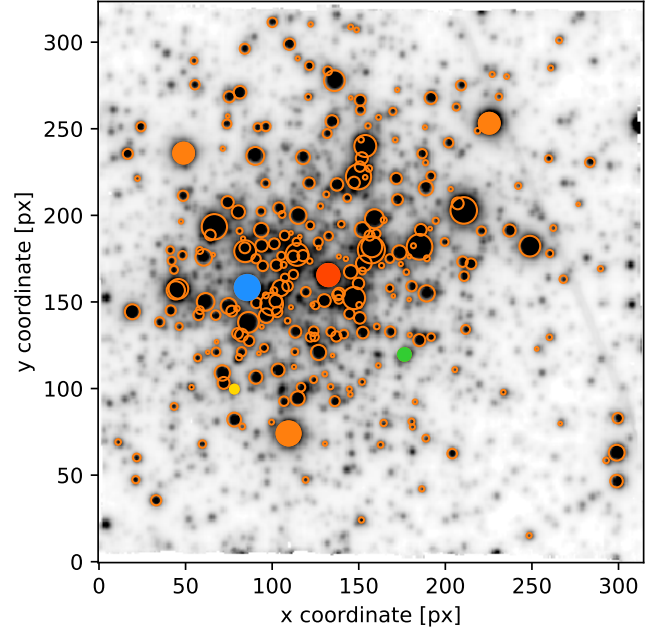


Fig. 5. Stars contained in the final target list (i.e., stars brighter than 18.5 in $F555W$) are overplotted in orange over the MUSE white-light image. The size of the circle corresponds to their inferred brightness in the V band. The stars marked with orange filled circles are used to fit the PSF (see Sect. 3.2). The spectra of the stars marked with red, blue, green, and yellow filled circles are shown in Fig. 6.

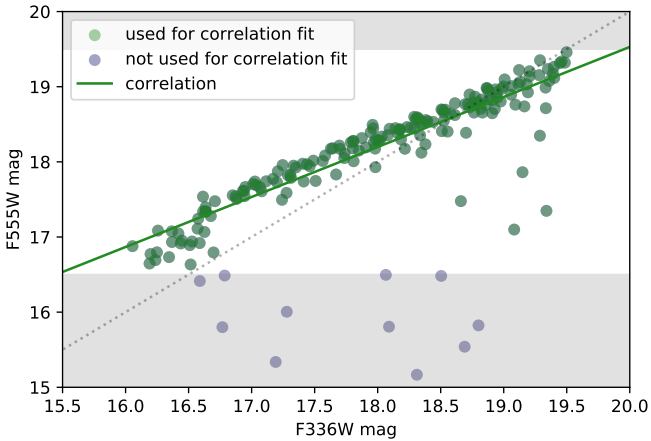


Fig. 4. Correlation between the HST $F336W$ ($\sim U$ -band) and $F555W$ ($\sim V$ -band) magnitudes. In order to fit the linear correlation (green line), we exclude stars with $F555W$ fainter than 19.5 (see Sect. 3.1) and brighter than 16.5 (gray regions). Stars that are brighter in $F555W$ but not in the UV are RSGs and therefore not included in the fit. The relation is used to convert $F336W$ magnitudes into $F555W$ magnitudes for all stars in the HST input catalogs. The gray dotted line indicates the one-to-one relation.

list described in Sect. 3.1, containing the 278 brightest stars. Subsequently, an effective PSF model (Anderson & King 2000) was derived from a selected set of isolated stars (see Fig. 5). Slice by slice (i.e., wavelength by wavelength), this PSF model was fit to each source, while the positions taken from the input list were held fixed. In this way, we determined the total flux and flux error of a given star in each slice. All fluxes and error values for each star were then concatenated to a spectrum.

We took the crowding of the field into account by simultaneously fitting the PSF of stars that were closer together than 12 pixels (corresponding to $2.4''$). An example of the extraction of spectra for deblended sources is shown in Appendix A. We were unable to extract spectra for seven stars because of the severe crowding. In total, we extracted spectra for 271 stars brighter than $V = 18.5$ mag.

3.3. Normalization

After automatically extracting the spectra of the brightest stars, we normalized them in an automatic manner. The normalization was performed for all spectra except for those of RSGs, which require special treatment because they have so many spectral lines.

To normalize the spectra, the continuum has to be determined and fit with a polynomial. For this, spectral lines have to be identified and excluded from the fit. This continuum search is based on a two-step process adapted from Sana et al. (2013). First, a minimum–maximum filter and a median filter are compared in a sliding window of a given size. If the value in the min–max filter exceeds the value of the median filter by a threshold value that depends on the S/N of the spectrum, a spectral line or cosmic hit is detected and the point is excluded from the fit. A polynomial is fit to this preliminary continuum. Points are excluded from the continuum points if they lie farther away than a second threshold value from the polynomial fit, and a new polynomial is fit through the remaining continuum points. This procedure is repeated in an iterative manner.

We considered the blue and red parts of the spectrum (i.e., wavelengths below and above the blocked laser-contaminated region between 5780 and 5990 Å) independently. Furthermore, in the wavelength region dominated by the Paschen lines, continuum flux was determined in fixed wavelength windows.

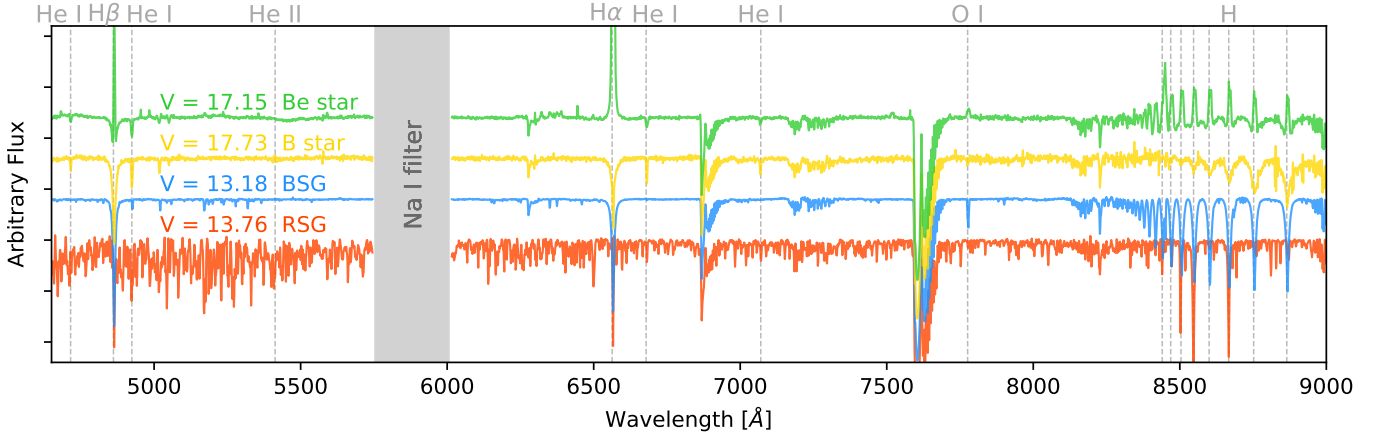


Fig. 6. Example spectra for different stars. From top to bottom: spectrum of a Be star (green), a B star (yellow), a BSG (blue), and an RSG (red). Our automated normalization mechanism was not applied to the RSG; it was normalized manually. The estimated V -band magnitude is given for each star. Important diagnostic lines are indicated. The gray shaded region indicates the wavelength region that is blocked by the sodium filter. The spectra are not corrected for tellurics.

Normalized example spectra for a Be star, a B star, an RSG, and a BSG are shown in Fig. 6. The estimated V -band magnitude is indicated in the plot. Using this method, we achieved a normalization accuracy of around 2.5% for all the spectra. The average S/N is greater than 400 for the BSGs and varies between 300 for the brightest and 80 for the faintest B stars in our sample.

4. Automated spectral classification

4.1. Main-sequence stars

Commonly used spectral classification schemes are based on the blue part of the spectrum, that is, on wavelengths below 4600 Å (Conti & Alshuler 1971; Walborn & Fitzpatrick 1990). Unfortunately, this region is not covered by the MUSE extended setup (see Sect. 2.1), and thus standard schemes cannot be applied to our case. Because our dataset contains so many stellar spectra, we aimed for an automated procedure that is reproducible and independent of human interaction.

We developed a new classification scheme for OBA main-sequence stars in the red part of the spectrum that is based on the relation between spectral type and the equivalent width (EW) of spectral lines. Similar approaches were proposed by Kerton et al. (1999) or Kobulnicky et al. (2012), for example, and were applied to MUSE data by Zeidler et al. (2018) and McLeod et al. (2019). While Kerton et al. (1999) focused on earlier spectral types between O5 and B0, Kobulnicky et al. (2012) used line ratios including the He I λ 5876 line, which is covered by the Na I filter in our data. Their classification can thus not be applied to our case.

We selected different diagnostic lines by focusing in particular on He II λ 5412, He I λ 6678, and the O I triplet centered around λ 7774. EWs are not altered by stellar rotation or extinction and can be measured in a consistent manner at MUSE resolution.

In order to calibrate the classification scheme, we used the standard stars listed in Gray & Corbally (2009). For all stars, observations obtained with the HERMES spectrograph mounted at the Mercator telescope in La Palma (Raskin et al. 2011) are available. HERMES is a high-resolution spectrograph providing spectra with $R = 85\,000$. All classification spectra have an $S/N > 150$. Because of the lack of late-O and early-B

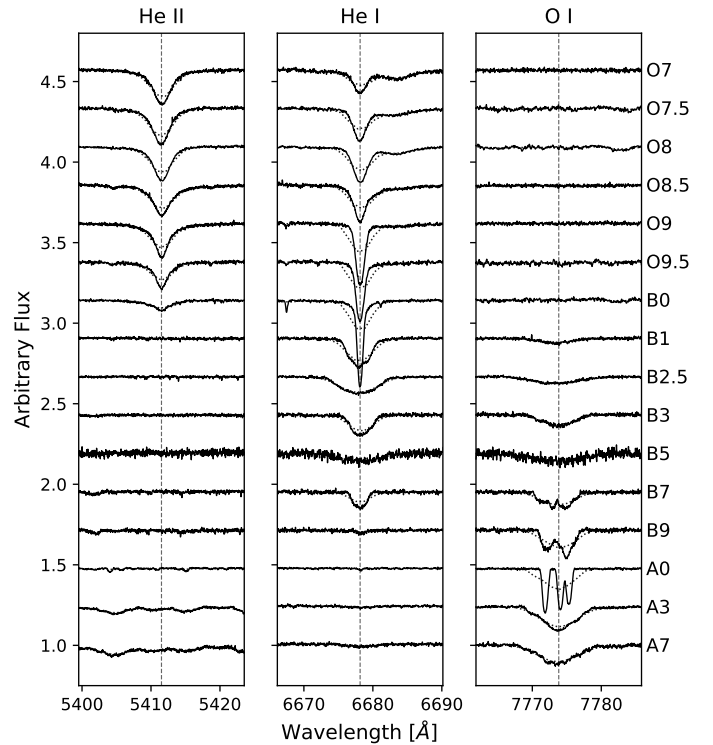


Fig. 7. Atlas of spectral standards listed in Table 1 around the three lines of interest. The spectra are shifted horizontally according to the radial velocity and vertically for clarity. The black line shows the original spectra, and the dotted line indicates the spectra degraded to MUSE resolution.

spectral standard stars in Gray & Corbally (2009), we complemented the list with the O-star spectral atlas by Sana et al. (in prep.). The O-star spectra used were observed with the Fibre-fed Extended Range Optical Spectrograph (FEROS, Kaufer et al. 1999) mounted at the 2.2 m Max-Planck-ESO telescope in La Silla, Chile, which has a resolving power of 48 000. In a handful of cases, both HERMES and FEROS observations are available for the same star. In these cases, we used the higher resolution, higher S/N HERMES spectra. All spectra used for the calibration are shown in Fig. 7 as a sequence of spectral type.

An overview of all calibration stars, their spectral types as listed in Gray & Corbally (2009) or Sana et al. (in prep.), and possible additional classifications are listed in Table 1. Some stars show variable spectra. Several are single- or double-lined spectroscopic binaries or known pulsating stars. After downgrading the spectra to MUSE resolution, we inspected the classification spectra to search for obvious contamination caused by the variability described above. In almost all cases, these are washed out by the low resolution. Only ν Ori (BOV) shows a composite spectrum typical of a double-lined spectroscopic binary comprising an early-type ($T_{\text{eff}} \approx 20\,000$ K) and a later-type star ($T_{\text{eff}} \leq 15\,000$ K). It is thus not further considered in our classification.

For all the standard stars we measured the EW and the corresponding error σ_{EW} in a 16 \AA wide window w around the center of the three lines mentioned above. The errors were estimated following Chalabaev & Maillard (1983):

$$\sigma_{\text{EW}} = \frac{\sqrt{2 \cdot w \cdot \Delta\lambda}}{S/N}, \quad (3)$$

where the S/N is the signal-to-noise ratio of the continuum close to the considered line and $\Delta\lambda$ is the wavelength step (i.e., 1.25 \AA for MUSE). We used these measured EWs to fit a second-degree polynomial, which provides the relation between EW and spectral type.

We repeated the measurements with degraded standard star spectra in which we adopted the resolution of MUSE and applied a typical S/N to the standard star data. While the relations themselves did not change, we used these measurements to investigate the limit for which genuine spectral lines can be distinguished from noise in the continuum. Given our data quality, this limit is 0.1 \AA . EW values were only considered for the relation fit when they were larger than this limit. Figure 8 shows the relations between EWs and spectral type for all three considered lines.

A special case is the He II line at 5412 \AA . In late-type stars (i.e., A3 and later), metal lines start to dominate in the considered wavelength regime, and especially the Fe I ($\lambda 5410.9 \text{ \AA}$) and the Ne I line ($\lambda 5412.6 \text{ \AA}$) contribute to EW measurements (marked with blue triangles Fig. 8). We therefore excluded these points from the relation fit at late spectral type. Tuesday, December 31, 2019 at 11:22 am The derived relations between a fractional spectral type (x_{Spt}) and the EW in \AA for the considered lines are

$$x_{\text{Spt}} = -\frac{0.4402 - \sqrt{0.3215 - 0.3905 \cdot \text{EW}_{5412}}}{0.1952}; \quad x_{\text{Spt}} \in [-3, 0] \quad (4)$$

$$x_{\text{Spt}} = -\frac{0.0360 - \sqrt{0.0152 - 0.0195 \cdot \text{EW}_{6678}}}{0.0098}; \quad x_{\text{Spt}} \in [-3, 9] \quad (5)$$

$$x_{\text{Spt}} = +\frac{0.0809 - \sqrt{0.0075 - 0.0096 \cdot \text{EW}_{7774}}}{0.0048}; \quad x_{\text{Spt}} \in [0, 17], \quad (6)$$

in which we consider a linear translation of spectral type to x_{Spt} , where B0 corresponds to $x_{\text{Spt}} = 0$ and B9 to $x_{\text{Spt}} = 9$.

Figure 8 shows these results graphically: the differentiation between early B- and late O-type stars is per definition the presence of significant He II lines. The EW of the He II line at 5412 \AA can thus be used as classifier for the presence of O stars in our sample. As He I lines are present in late O- to late B-type stars, our second relation can be extrapolated to spectral type B9 and thus be used for stars O7-B9. Finally, the O triplet at 7774 \AA is present in spectral types later than B3 (up to A7).

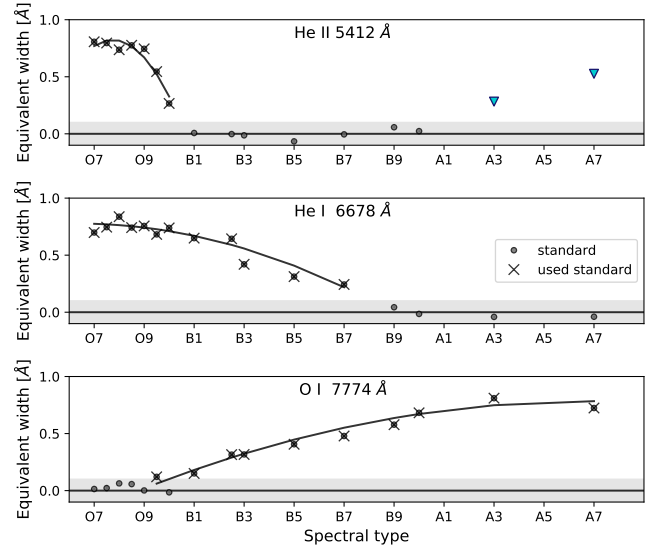


Fig. 8. From top to bottom: correlation between the EW measured in the standard star spectra and their spectral type for He II $\lambda 5412$, He I $\lambda 6678$, and the O I triplet at $\lambda 7774$. Black dots show the measured values, and black crosses indicate the data points used to fit the polynomial. EW measurements below 0.1 \AA (shaded region around the black line at 0 \AA) do not allow a significant detection of spectral lines from noise in the continuum and are therefore excluded from the fit. In the special case of the He II line, the EWs at late spectral types (A5 and later), which are contaminated by metallic lines and thus were not considered in the fit, are indicated by blue triangles.

The derived relations are based on the standard star spectra of galactic stars and are not corrected for the effect of metallicity. Because NGC 330 lies in the SMC, that is, at significantly lower metallicity, the O I line is weaker in our sample than predicted by the galactic standard stars. Because the effect of metallicity is negligible for the He I and He II lines, we focused on these lines to determine spectral types in the MUSE data.

The strength of the O I triplet at $\lambda 7774$ is sensitive to temperatures covered by later spectral types, that is, especially to A-type stars where the He I $\lambda 6678$ line is no longer present. In order to be able to detect possible A-type stars, we first classified all stars with a particular focus on the O I line. We did not detect any spectrum that showed O I lines and no He I, that is, there are no A-type MS stars in the sample. The only cases where O I is present in the spectra also show strong He I lines, a signature that is indicative of the composite spectra of spectroscopic binaries (see Sect. 4.4).

The classification using the He II and He I lines was applied to all B-type MS stars and yields fractional spectral types interpolated from the relations described above. Taking the errors into account, we achieve an accuracy of about one spectral subtype. An overview over the derived values is given in Appendix D. An example diagnostic plot showing the measured EW for one star (star 654) and the derived spectral type is given in Fig. 9. For comparison reasons, Fig. 10 shows the classification of the same star by eye. Both methods agree within their errors.

Because it is difficult to distinguish dwarf and giant luminosity classes based on the low resolution of the MUSE data, we derived the automated classification scheme for MS stars alone, implicitly assuming that all stars except for supergiants are on the MS. We applied this to all sample stars except for supergiants (which are several magnitudes brighter and clearly identifiable in the MUSE data, see Sect. 4.2). In addition to RSGs and BSGs, the automatic approach to classification reveals its limitations for

Table 1. OBA spectral standards from [Gray & Corbally \(2009\)](#) and Sana et al. (in prep.).

Classification	Identifier	v_{rad} [km s ⁻¹]	Additional information	References
O7V	15 Mon	22.0	Oe star, SB2 (O7Ve + O9.5n)	Gies et al. (1993)
O7.5Vz [†]	HD 152590	0.0	Eclipsing binary, SB2	Sota et al. (2014) , Sana et al. (in prep.)
O8V [†]	HD 97848	-7.0	-	Walborn (1982) , Sota et al. (2014) , Sana et al. (in prep.)
O8.5V	HD 46149	45.9	SB2 (O8.5V + B0-1V)	Mahy et al. (2009) , Sana et al. (in prep.)
O9V	10 Lac	-10.1	-	Sota et al. (2011)
O9.5V [†]	HD 46202	53.0	-	Sota et al. (2011) , Sana et al. (in prep.)
B0.2V [†]	τ Sco	2.0	Magnetic star	Donati et al. (2006)
B1V [†]	ω Sco	-4.4	Variable star of β Cep type	Telting & Schrijvers (1998) , Sana et al. (in prep.)
B2.5V(n) [†]	22 Sco	0.0	-	Bragança et al. (2012) , Sana et al. (in prep.)
B3V	η Aur	7.3	-	Morgan & Keenan (1973)
B5V	HD 36936	18.7	-	Schild & Chaffee (1971)
B7V	HR 1029	-1.5	Pulsating variable star	Grenier et al. (1999) , Szewczuk & Daszyńska-Daszkiewicz (2015)
B9V	HR 749A	9.7	-	Gray & Corbally (2009)
A0Va	α Lyr	-20.6	Variable star of δ Sct type	Gray et al. (2003) , Böhm et al. (2012)
A3V	β Leo	-0.2	Variable star of δ Sct type	van Belle & von Braun (2009) , Bartolini et al. (1981)
A7V	HR 3974	-11.4	Variable star of δ Sct type	Gray et al. (2003) , Rodriguez et al. (1991)
A0 Ia	HR 1040	-6.2	Evolved supergiant star	Bouw (1981) , Gray & Garrison (1987)
A0 Ib	η Leo	1.4	-	Cowley et al. (1969) , Lobel et al. (1992)
A0 III	α Dra	-13.0	SB1	Cowley et al. (1969) , Levato (1972) , Bischoff et al. (2017)

Notes. The radial velocities (Col. 3) and additional information (Col. 4) are taken from references indicated in Col. 5. Stars marked with a dagger are listed in Sana et al. (in prep.). The top part of the table contains MS standard stars (see Sect. 4.1), and the bottom part lists giant and supergiant standards (see Sect. 4.2).

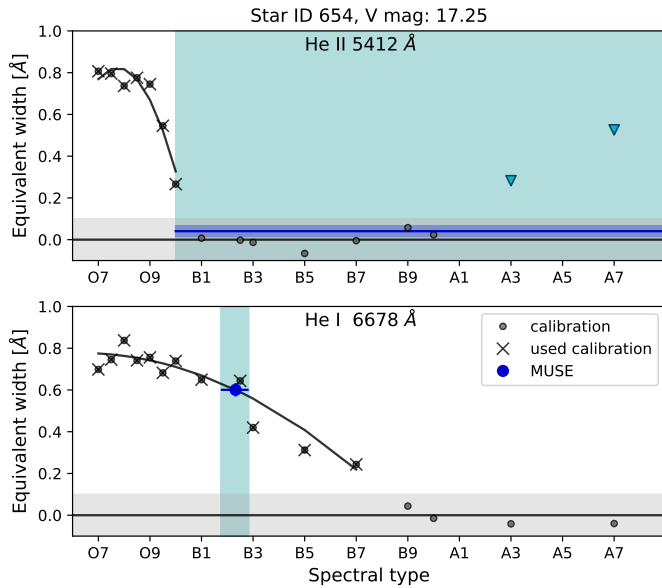


Fig. 9. Equivalent width measurements for star 654 overplotted on the fit relations described in Eqs. (4) and (5). As mentioned above, we focused on the He lines to determine the spectral type. The blue shaded region indicates the allowed range of spectral types given the measured EWs with corresponding errors. Using this automated method, we determine a spectral type B2 with an accuracy of about one subtype. See also Fig. 10.

Be stars and spectroscopic binaries with a composite spectrum. The identification and classification of these stars is described in the following sections.

4.2. Red and blue supergiants

Red and blue supergiants are identified based on their brightness: they are several magnitudes brighter in the V band than the MS stars. We find 11 bright red and 6 bright blue stars in

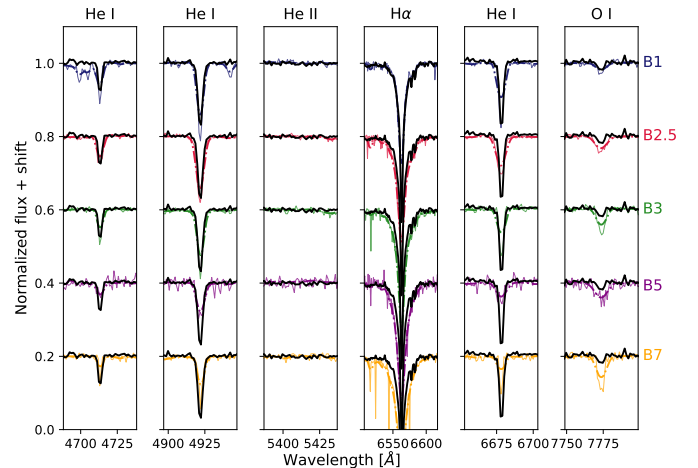


Fig. 10. By-eye classification of star 654. The stellar spectrum (in black) is compared to five standard stars, downgraded to the MUSE resolution. The continuous lines show the original spectra, and the dash-dotted lines show the spectra rotationally broadened by 200 km s⁻¹. By eye, the star would be classified as B1-B2 star, which agrees with the automatically derived spectral type of B2 \pm one subtype. See also Fig. 9.

the cluster core. Focusing on the bright red stars, [Patrick et al. \(2020\)](#) checked cluster membership based on *Gaia* DR2 proper motion and parallax measurements ([Gaia Collaboration 2018](#)). They find that 4 stars have less reliable *Gaia* data and might be potential Galactic contaminants. Their radial velocities, however, agree well with the SMC radial velocity. The uncertainties in *Gaia* DR2 parallaxes for the bright blue stars are large, therefore we assessed SMC membership by measuring their radial velocities, which are all in good agreement with the radial velocity of the SMC. In total, the cluster core contains 11 RSGs and 6 BSGs.

In order to verify that the stars are supergiants rather than giants, we calculated their absolute V magnitude using the

distance modulus $m - M = 5 \log d - 5 + A_V$, assuming a distance of 60 kpc and an extinction of $E(B - V) = 0.08$ (Keller et al. 1999; Lennon, priv. comm.). As shown in Table 2, the V -band magnitudes of the RSGs and BSGs are between 12.6 and 14.1. This gives absolute magnitudes between -6.5 and -5.0 , which is in the range of expected absolute magnitudes for bright A-type giants and A-type supergiants.

The 11 RSGs in NGC 330 are studied in greater detail in Patrick et al. (2020), who derive spectral types following the classification criteria and method detailed in Dorda et al. (2018). We adopted their spectral type classifications and include them in Table 2.

To classify the six blue supergiants, we used a second set of standard star spectra of different luminosity class from Gray et al. (2003) that were observed with the HERMES spectrograph. Standard star spectra are available for spectral types B5, A0, and A7 and include luminosity classes Ia, Ib, and III.

When we classified the blue supergiants from the MUSE data, we first determined the spectral type based on He I lines and then estimated the luminosity class based on the width of the Balmer lines. As explained above, the strength of metallic lines cannot be used for classification because of the lower metallicity of the SMC. Given the availability of the classification spectra, we give a wide spectral type estimate of late-B, early-A and late-A.

Five of the six blue supergiants are early-A stars and one is a late A-type star. While one star has luminosity class Ia-Ib, all the other supergiants are of luminosity class Ib-III. One example for the spectral classification of an A-type supergiant is shown in Fig. 11.

Three of the A-type supergiants have previously been studied by Feast & Black (1980) and Carney et al. (1985). Their spectral types agree with those derived in this study within the errors. Two blue supergiants have not been mentioned in literature before. Table 2 gives a summary of all the parameters of the RSGs and BSGs derived here compared to literature values.

4.3. Be stars

Classical Be stars are rapidly rotating B-type stars with Balmer lines as well as other spectral lines from OI and HeI, for instance, in emission, which arise from a circumstellar decretion disk (Rivinius et al. 2013). Different possible origins for the rapid rotation of Be stars have been proposed. Be stars might be born as rapid rotators (Bodenheimer 1995; Martayan et al. 2007b). They might also become rapid rotators during their MS evolution, either as single stars (Ekström et al. 2008) or due to transfer of mass and angular momentum in a binary system (Packet 1981; Pols et al. 1991; Vanbeveren & Mennekens 2017). The strength of the emission lines is variable on timescales of months to years and strongly depends on the disk density and inclination angle (see, e.g., Hanuschik et al. 1988). Next to $H\alpha$, the $OI\lambda 7774$ line is most strongly affected by the infilling due to disk emission and often appears completely in emission.

In addition to automatically deriving a spectral type from the EW of the He I line, we therefore compared the spectra of all Be stars to standard star spectra of B-type MS stars by eye, where a stronger focus was placed on all available He I lines. We achieved an accuracy with the visual inspection method of up to about three spectral subtypes. One example of this method of classification is shown in Appendix B. Both methods agree within the errors for a majority of the stars in the sample. When the methods disagreed, we kept the spectral type that was derived

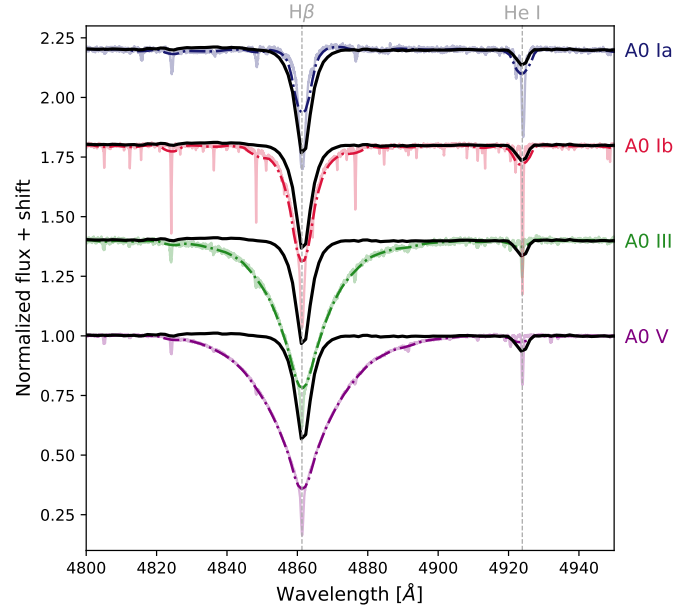


Fig. 11. Spectral classification of an A-type supergiant (star 729). The MUSE spectrum (in black) is compared to four standard star spectra of spectral type A0 Ia, A0 Ib, A0 III, and A0 V. The continuous line shows the original spectra, and the dash-dotted lines show the spectra rotationally broadened by 200 km s^{-1} . All standard star spectra are downgraded in resolution to match the MUSE data. We classify this star as early A-type star with luminosity class Ia-Ib.

through visual inspection because it allowed us to take more spectral lines into account.

Both methods, however, are based on the strength of the He I lines, which grow in strength with earlier spectral types. As they may suffer from infilling and thus appear less deep than they actually are, a systematic shift in classification toward later spectral types is possible. The estimated spectral types are therefore a lower limit in terms of spectral type.

In total, we find Balmer line emission in 82 of the 251 MS stars in the sample. This gives a lower limit on the observed Be star fraction in our sample of $f_{\text{Be}} = 32 \pm 3\%$. While most of the emission-line stars are of mid- to late B-type, we find one O9.5eV and one O9.5/B0eV star in the sample. Both stars show clear absorption in the He II line at $\lambda 5412$. Their spectra are shown in Fig. 12.

4.4. Spectroscopic binaries

We only consider one epoch in this study, therefore we cannot rely on radial velocity variations to detect spectroscopic binaries. Nevertheless, we find indications for binarity in some of the spectra. For some stars we see strongly asymmetric lines that consist of two line components of different radial velocity. Other spectra appear to be composite spectra that show deep He I lines, which are indicative of an early spectral type, and deep OI lines, which are characteristic for a later spectral type.

Composite spectra could also occur when two sources are so close in the plane of the sky that their spectra are extracted together. The spectral extraction using PSF fitting based on the higher spatially resolved HST data as input catalog takes this into account. Other possible explanations of the observed line shapes might be, for example, different micro- or macroturbulence values that affect lines differentially. A higher oxygen abundance could lead to a stronger OI line. A more certain classification as

Table 2. Overview of the parameters of the red and blue supergiants from this paper and from the literature.

Identifier			α	δ	V mag	Spectral type			
This work	A59	R74	J2000	J2000	R74	This work	P2019	FB80	C85
614	II-26	A3	00:56:21.670	-72:27:35.859	13.8	–	G3 Ib	–	–
732	II-43	A6	00:56:13.895	-72:27:32.402	13.5	–	K1 Iab	–	–
731	II-41	A7	00:56:14.562	-72:27:42.451	13.0	–	G6 Ib	–	–
452	II-42	A9	00:56:12.861	-72:27:46.631	14.1	–	K1 Ib	–	–
724	II-17	A14	00:56:19.037	-72:28:08.237	13.5	–	K1 Ib	–	–
619	II-32	A27	00:56:17.083	-72:27:35.011	13.9	–	K1 Ib	–	–
446 ^(*)	II-21	A42	00:56:20.142	-72:27:47.094	13.9	–	K0 Ib-II	–	–
727 ^(*)	II-38	A45	00:56:18.828	-72:27:47.498	13.8	–	G3.5 Ia-Iab	–	–
367	II-37	A46	00:56:18.016	-72:27:49.852	13.8	–	K0 Ib	–	–
428 ^(*)	II-36	A52	00:56:17.371	-72:27:52.530	13.6	–	K0 Ib	–	–
280 ^(*)	II-19	A57	00:56:19.472	-72:27:53.220	13.6	–	G7 Ia-Iab	–	–
333	II-16	A16	00:56:21.947	-72:27:51.15	13.1	early A Ib-III	–	B9 I	A2 I
335	II-20	A41	00:56:20.186	-72:27:50.99	13.2	early A Ib	–	–	–
729	II-35	A47	00:56:17.002	-72:27:46.49	12.6	early A Ia-Ib	–	B9 I	–
453	II-40	A29	00:56:15.811	-72:27:46.17	13.1	early A Ib-III	–	–	–
503	II-23	A19	00:56:21.022	-72:27:43.92	13.1	late A Ib	–	–	–
586	II-33	A25	00:56:17.340	-72:27:38.13	13.1	early A Ib-III	–	A1 I	A0 I

Notes. Literature identifications are from [Arp \(1959, A59\)](#) and [Robertson \(1974, R74\)](#). Literature spectral types are from [Patrick et al. \(2020, P2019\)](#), [Feast & Black \(1980, FB80\)](#), and [Carney et al. \(1985, C85\)](#). ^(*)Identifies potential Galactic contaminants based on *Gaia* data.

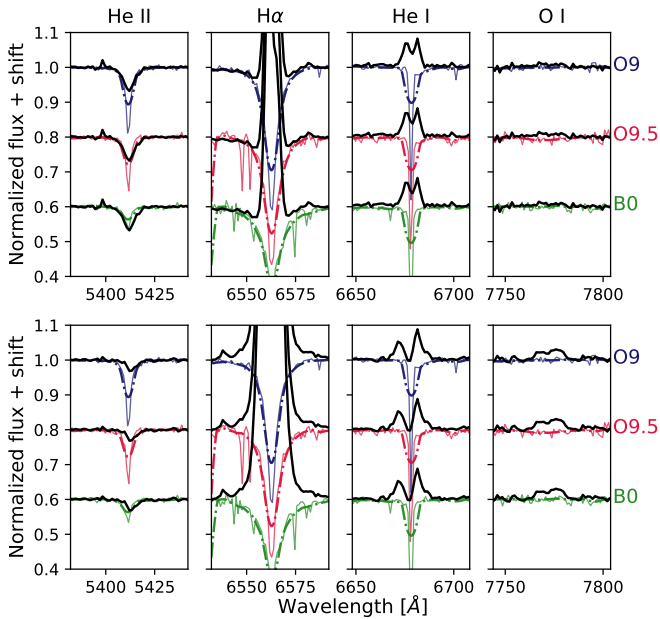


Fig. 12. Spectral classification of the O9.5e star (star 420, *upper panel*) and the O9.5/B0e star (star 432, *lower panel*). The two stellar spectra (in black) are compared to three standard star spectra of spectral type O9, O9.5, and B0 in blue, red, and green (described in Sect. 4.1), downgraded to MUSE resolution. The continuous line shows the original spectra, and the dash-dotted line shows the spectra after rotational broadening by 200 km s⁻¹ was applied.

spectroscopic binary will only be possible when periodic radial velocity shifts are detected.

In total, we find 36 candidate spectroscopic binaries in our sample. If this includes no false positive due to the possible reasons mentioned above, this would imply a lower limit on the observed spectroscopic binary fraction of $f_{\text{binary}} = 14 \pm 2\%$. One example spectrum is shown in Fig. 13. A more thorough investigation of the spectroscopic binaries will follow in Paper II of

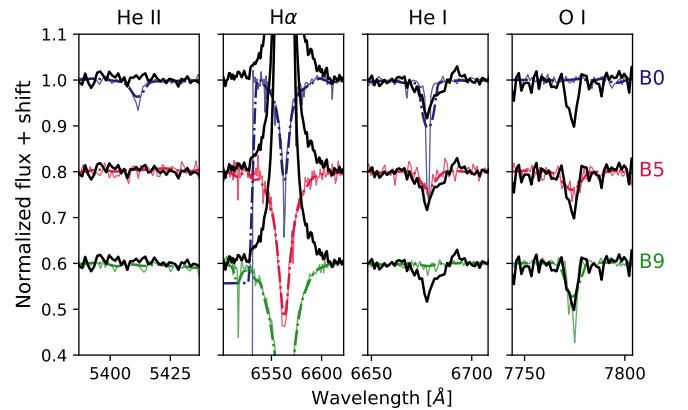


Fig. 13. Composite spectrum of the spectroscopic binary star number 50. The spectrum of the star (in black) is compared to three standard star spectra of spectral type B0, B5, and B9 in blue, red, and green, respectively (described in Sect. 4.1), downgraded in resolution to match the MUSE data. The continuous colored line shows the original spectra, and the dash-dotted line shows the spectra after rotational broadening by 200 km s⁻¹ was applied.

this series, where we will use all available six epochs to measure radial velocities for all stars.

5. Stellar content of NGC 330

5.1. Spectral types

Out of the 278 stars brighter than $V = 18.5$ mag, there are 249 B-type stars, 2 O-type stars, 11 RSGs, and 6 A-type supergiants. For 7 stars, the extraction of a sufficiently uncontaminated spectrum was not possible, and 3 stars appear to be foreground stars. Eighty-two of the MS stars show Balmer line emission and are classified as Be stars. A distribution of spectral subtypes for B and Be stars is shown in Fig. 14. Most of the stars are of spectral type B3 to B6. There are only a few stars with spectral type

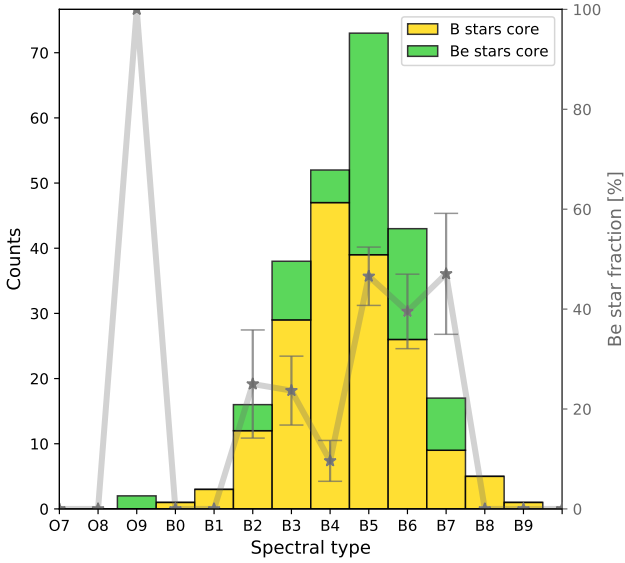


Fig. 14. Distribution of spectral types for MS stars, where yellow indicates B stars and green indicates Be stars. The left axis shows the total number of stars, while the right axis indicates the Be star fraction in each bin. The accuracy of spectral type determination is about one spectral subtype. Overplotted is the Be star fraction in each bin, for which we give counting errors, except for cases where the Be star fraction is 0 or 100%.

B2 and earlier and only one O-type and one O9/B0 star (both are in fact Oe/Be stars). The lack of later spectral types, that is, of late-B and A-type stars, is probably due to the cut in brightness that we applied when the spectra were extracted (i.e., only stars with $V < 18.5$ were considered).

The spatial distribution of all stars is shown in Fig. 15. While B-type stars seem to be evenly distributed, the Be stars seem to be clustered in the southeast part of the cluster core (i.e., the lower left corner of the image). Red and blue supergiants are mostly found in the inner region of the cluster.

A handful of stars in our sample were studied by Grebel et al. (1996), Evans et al. (2006), and Martayan et al. (2007a). The two stars studied by Grebel et al. (1996) have similar spectral types but different luminosity classes and were classified as Be stars by them, but they show no signs of emission in our spectra (star 41 = Arp II-4 was as B2-3Ve star, while we classify it as a B3V star; star 670 = Arp II-31 was classified as B2-3 Iie star, while we classify it as a B5 V star). This might either be due to the variable nature of the Be star phenomenon, or it might be caused by $H\alpha$ contamination in the spectra used by Grebel et al. (1996).

Our derived spectral types for the two stars scrutinized by Evans et al. (star 57 = NGC 330-036 and star 654 = NGC 330-095), are within the error bars: we classify star 57 as B3, while it is listed as B2 II star in Evans et al. (2006), and star 654 as B2, which by them is listed as B3 III star.

Furthermore, there are six stars in common with the sample of Martayan et al. (2007a), which are classified as early-Be stars (B1e-B3e). For these stars (stars 723, 127, 205, 254, 661, and 667), we find a systematically later spectral type between B3e and B6e. This systematic difference could be due to their different classification methods: while we determined spectral types based on the EW of diagnostic spectral lines and by visual comparison to standard star spectra, Martayan et al. estimated T_{eff} and $\log g$ from the spectra and transcribed these into spectral types and luminosity classes adopting the galactic calibrations

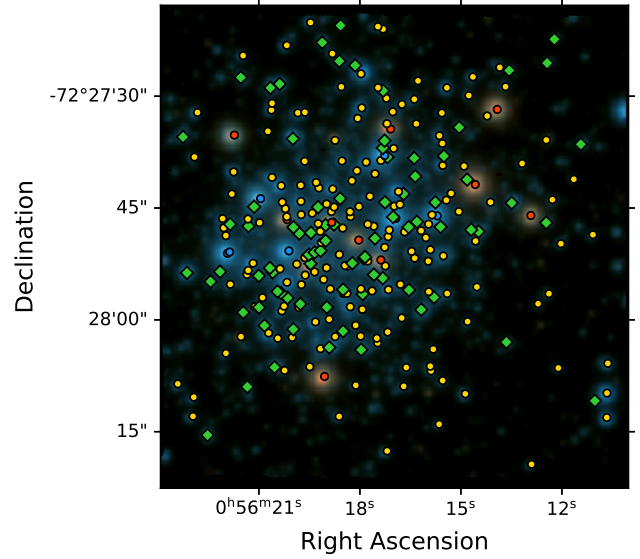


Fig. 15. Stellar classification for all 275 stars with $V < 18.5$ mag overplotted on a MUSE RGB image created from the B , V , and I filters. B stars are marked with yellow circles, Be stars with green diamonds, RSGs with red circles, and BSGs with blue circles.

by Gray & Corbally (1994) for B stars and those by Zorec et al. (2005) for Be stars.

5.2. Color magnitude diagram

We used the HST photometry published in Milone et al. (2018)³ to reconstruct their color magnitude diagram (CMD) from the HST $F336W$ and $F814W$ bands (see Fig. 16) and cross-correlated it with our MUSE data to include the spectral type information we obtained from the spectra. The HST observations contain about 20 000 sources that cover a significantly larger area than the MUSE FoV. In addition to NGC 330 cluster members, the data probably contain several field stars as well as foreground stars (i.e., in lower right part of the CMD). Several of our brightest stars, that is, two A-type supergiants and six RSGs, are missing in the HST catalog. We therefore cannot include them in the CMD.

We confirm the findings of Milone et al. (2018), who reported a high fraction of stars with $H\alpha$ emission, which they interpreted as Be stars (taking into account narrow-band F656N observations). Furthermore, they found a split MS near the cluster turnoff, which they understood as a signature of multiple stellar populations in the cluster. Using the MUSE spectra, we confirm that the red MS consists of Be stars with $H\alpha$ emission. This might be because the Be star phenomenon preferentially occurs at or close to the terminal age MS (Martayan et al. 2010). It might also be a temperature effect due to the rapid rotation of these stars. According to Townsend et al. (2004), rapidly rotating stars may indeed appear cooler, translating into a classification of up to two spectral subtypes later. This effect is also visible in Fig. 14.

Following Milone et al. (2018), we overplot single-star non-rotating Padova isochrones (Bressan et al. 2012; Chen et al. 2014, 2015; Tang et al. 2014; Marigo et al. 2017; Pastorelli et al. 2019)⁴. We adopted the standard values for the SMC, that is,

³ Online available at <http://progetti.dfa.unipd.it/GALFOR/>

⁴ Obtained from <http://stev.oapd.inaf.it/cgi-bin/cmd>

the distance of $d = 60$ kpc (Harries et al. 2003; Hilditch et al. 2005; Deb & Singh 2010), the metallicity $Z = 0.002$ (Brott et al. 2011), the foreground extinction $E(B - V) = 0.08$ (Keller et al. 1999; Lennon, priv. comm.), and the SMC extinction law by Gordon et al. (2003), and considered isochrones for ages between 30 and 45 Myr. While we find a good agreement of the isochrones of 35 and 40 Myr with the uppermost part of the MS, none of the isochrones reproduces the fainter end of the MS (stars fainter than $F814W = 20$, not included in Fig. 16, but see Appendix C for a zoomed-out version). They are systematically too faint by ≈ 0.3 mag.

This effect can also be seen in the CMDs showed in Milone et al. (2018) and Sirianni et al. (2002). While Sirianni et al. (2002) used different HST data and different isochrones from Schaerer et al. (1993), we used the data from Milone et al. (2018) and the same Padova isochrones with slightly different input values (i.e., they adopted $d = 57.5$ kpc, $E(B - V) = 0.11$, and a galactic extinction law). Trying to reproduce their findings using the same input values, we find that the shape of the isochrones is slightly different. This might be due to updates in the codes used to derive the isochrones (several updates were released in 2019, including a new version of the code producing isochrones, Marigo et al. 2017).

When we fit the isochrone, we therefore focus on the upper part of the B-star MS, which is best reproduced by the isochrones at 35 and 40 Myr. The isochrones at 30 and 45 Myr do not fit the top part of the stars (see also Fig. C.1). This leads to an age estimate of 35–40 Myr. We note that the isochrones reproduce the position of the RSGs and BSGs in the CMD very well.

Patrick et al. (2020) estimate the age of NGC 330 based on the population of RSGs (see also Britavskiy et al. 2019). They find a cluster age of 45 ± 5 Myr, which agrees well with what is presented here. This is expected given how well the isochrone fitting method reproduces the location of the RSGs in Fig. 16.

We find the cluster turnoff to be at $F814W \approx 16.5$ mag, which corresponds to $M \approx 7.5 M_{\odot}$, which is just below the limiting mass for neutron star formation. This indicates that all currently produced binary Be stars may remain in the cluster because their companions are likely white dwarfs.

Several stars in the CMD are brighter and hotter than the cluster turnoff, that is, they might be blue stragglers. Half of them are B stars and the other half are Be stars. These stars are expected to have gained mass in previous binary interactions. They are thus some of the best candidates for BiPs.

5.3. Be stars

The 251 B- and O-type stars include 80 Be stars and 2 Oe stars, indicating a lower limit on the Be star fraction of $f_{\text{Be}} = 32 \pm 3\%$. This fraction is high compared to typical Be star fractions of about 20% (Zorec & Briot 1997) measured in field or cluster stars in the Milky Way. The latter fraction is determined using several years of observations of bright galactic stars. Owing to the variability of Be stars and the disappearance of the emission lines on timescales of months or years (Rivinius et al. 2013), our fraction, which is based on one observational epoch, is a lower limit on stars that display the Be phenomenon.

Several previous studies derived high Be star fractions (about 50%) in NGC 330 (Feast 1972; Mazzali et al. 1996; Keller & Bessell 1998). However, these are based on small sample sizes and focus on stars in the outskirts of the cluster. Evans et al. (2006) studied a sample of 120 stars in the outskirts of NGC 330 (see Fig. 1) and find a Be fraction of $f_{\text{Be}} = 23 \pm 4\%$.

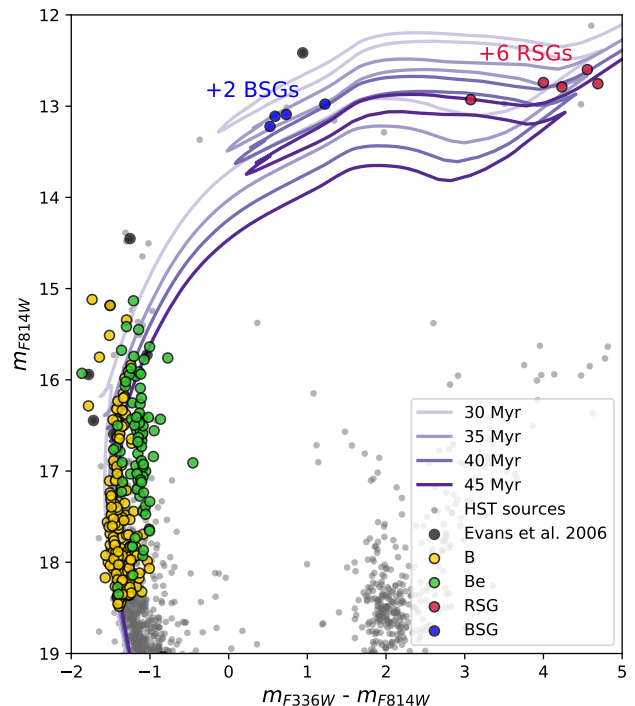


Fig. 16. Reconstructed CMD from Milone et al. (2018), where their complete input catalog containing field and cluster stars (see their Fig. 2) is shown in gray. The sources with available MUSE spectra are colored in terms of the spectral type we derived from the MUSE data, that is, Be stars in green, B stars in yellow, RSGs in red, and BSGs in blue. The eight sources studied by Evans et al. (2006) that are included in the HST data are indicated with black circles. Overplotted are single-star nonrotating Padova evolutionary tracks for ages between 30 and 45 Myr. Two A-type supergiants and six RSGs are missing in the HST catalog and thus cannot be included in this diagram.

Our detected Be star fraction is significantly higher than the fraction measured by Evans et al. (2006).

Interestingly, the two earliest-type stars in the sample have $H\alpha$, He I, and O I emission but also show He II absorption. They are classified as Oe/Be stars (see Sect. 4.3). Using the CMD, we identify them as blue stragglers, that is, BiP candidates.

As shown by the Be star fraction in Fig. 14, the spectral type distribution of Be stars seems to be bimodal, with a shift to later spectral types. As explained in Sect. 4.3, this could be due to the infilling of spectral lines by the emission component, which in particular leads to weaker He I lines and thus to a classification into a later spectral type. Additionally, rapidly rotating stars are likely to appear cooler and would subsequently be classified up to two spectral types later than a nonrotating star (Townsend et al. 2004).

In Fig. 17 we instead consider the fraction of Be stars as a function of HST magnitude ($F814W$) because this is less sensitive to these effects, assuming the population is coeval. It shows that the Be star fraction is between 50 and 75% for stars brighter than 17.0 mag in $F814W$ (corresponding to $7.0 M_{\odot}$, according to the Padova isochrones) and rapidly drops below 20% for stars fainter than 17 mag in $F814W$. This drop corresponds to the cluster turnoff at $F814W = 16.5$ mag (i.e., $M \approx 7.5 M_{\odot}$). We quantitatively estimate the effect of emission in the Paschen series on $F814W$ photometry from the MUSE spectra. We find that even the strongest Paschen emission series amounts to only ≈ 0.01 mag in the $F814W$ band, and hence is negligible.

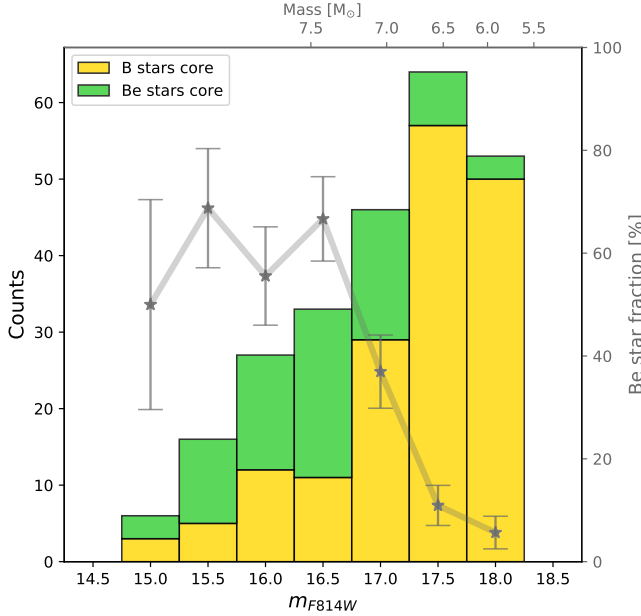


Fig. 17. Distribution of B and Be stars (in green and yellow, respectively) over F814 magnitude taken from Milone et al. (2018), where the left axis shows the total number of stars and the right axis indicates the Be star fraction in each bin. The top axis indicates the conversion from F814W magnitude into mass taken from the Padova isochrones. Stars brighter than $F814W = 16.5$ are above the cluster turnoff, where their mass remains mostly constant, but they increase in brightness.

We furthermore see a similar trend when we consider $F336W$ magnitudes instead of $F814W$ magnitudes in the histogram.

The lack of fainter Be stars could indicate the cutoff luminosity (or mass) for which B-type stars do not appear as Be stars anymore. This could either arise because these stars do not develop a disk, or because the ionizing flux emitted by these fainter stars is not high enough to ionize the Be star disk (Bastian et al. 2017).

A high-mass X-ray binary ([SG2005] SMC38) is reported within the MUSE FoV (Shtykovskiy & Gilfanov 2005; Sturm et al. 2013; Haberl & Sturm 2016). The region is crowded and the uncertainty in the position of the source is $0.7''$, which means that an unambiguous assignment to one of our sample stars is not possible. The two closest stars (i.e., within the errors of the XMM position) are stars 94 and 113, a B5Ve and a B4V star, respectively. In both cases, and given the position of the system in the cluster core, the massive but hidden companion may be a black hole. In the case of a neutron star, it is likely that the system would have been ejected in the supernova explosion. The distance of the SMC means that even at low kick velocities of $v_{\text{kick}} \leq 2 \text{ km s}^{-1}$, the system would have moved 20 pc within 10 Myr, which is out of the MUSE FoV. A more in-depth analysis of this object will follow in a subsequent paper of this series.

5.4. Estimate of the total mass of NGC 330

In order to estimate the total mass of NGC 330, we used the HST data to determine a scaling factor for the initial mass function (IMF) to the local star density of NGC 330. For this we need an estimate of the total stellar mass in a certain mass bin.

Following Milone et al. (2018), we defined the cluster core to have a radius of $24''$ and only considered stars within that distance from the center. Because the HST data cover a wider region than the MUSE data, we took a less crowded region toward the

edge of the HST data in order to estimate the contamination by field stars.

From the isochrone fit to the blue MS in the CMD (see Fig. 16), we count the number of stars between 3 and $5 M_{\odot}$ in the cluster as well as in the field region. We find that there are 412 stars between 3 and $5 M_{\odot}$, which corresponds to a total mass of $1650 M_{\odot}$ in this mass bin. In comparison, the mass of the field population in that same mass bin, which we subtracted from the cluster mass, is only $94 M_{\odot}$. Comparing this to the integrated IMF in the same mass bin gives us a scaling factor that scales the IMF to the local star density of NGC 330. Assuming a Kroupa IMF (Kroupa 2001) and the occurrence of stars with masses between 0.01 and $100 M_{\odot}$, we derive a total mass of the cluster of $M_{\text{tot,NGC 330}} = 88 \times 10^3 M_{\odot}$.

In order to estimate an error on the total cluster mass, we inspected the sensitivity of the estimate to the assumptions we made. The total cluster mass increases by 5% when we do not subtract the field population when we estimate the mass between 3 and $5 M_{\odot}$. While the mass estimate is not altered significantly by assuming a different high-mass end of the IMF, it depends strongly on the low-mass end: when we assume a low-mass end of $0.08 M_{\odot}$ (instead of $0.01 M_{\odot}$), the total cluster mass is 4% lower. The assumption that affects the estimate most is the assumed cluster radius, however. Increasing and decreasing the radius by 25% results in a total mass of $M_{\text{tot,NGC 330}} = 105 \times 10^3 M_{\odot}$ and $M_{\text{tot,NGC 330}} = 70 \times 10^3 M_{\odot}$, respectively. We thus take this as the dominating uncertainty, which results in a total cluster mass of $M_{\text{tot,NGC 330}} = 88^{+17}_{-18} \times 10^3 M_{\odot}$.

Mackey & Gilmore (2002) estimated a mass of $38 \times 10^3 M_{\odot}$ based on the surface brightness profile derived from archival HST data. McLaughlin & van der Marel (2005) found a similar value of $36 \times 10^3 M_{\odot}$. As an order of magnitude estimate, we agree with their mass estimate within a factor of two. Patrick et al. (2020) estimate the dynamical mass of NGC 330 based on the velocity dispersion of several RSGs and find a dynamical mass of $M_{\text{dyn}} = 158^{+76}_{-51} \times 10^3 M_{\odot}$, which is significantly higher than our estimate. The authors comment that this might be due to the effect of binarity on the determination of M_{dyn} .

5.5. Inner regions versus outskirts

Figure 18 compares the spectral type distribution of Evans et al. (2006) with a subsample of this work adopting the same magnitude cutoff, that is, $V < 17$ mag. This only leaves 22 MS stars in our sample. Significantly more early-type stars are included in the sample of Evans et al. (2006). This trend persists when we only include stars from Evans et al. (2006) that are closer than a certain distance from the cluster core, which reduces the probability of including field stars. This might be due to a systematic difference in spectral typing, although this is not supported by the two stars that are in common between the two samples (see Sect. 5). It might also indicate that the stars in the sample of Evans et al. are younger and more massive than the core population.

Furthermore, we find a significantly higher Be star fraction in the core than the outskirts. Restricting our sample to stars brighter than $V = 17$, which is the brightness limit of Evans et al., we find a Be star fraction of $f_{\text{Be}} = 46 \pm 10\%$, while the fraction detected by Evans et al. is $f_{\text{Be}} = 23 \pm 4\%$.

Another significant difference between the core and the outskirts is the different binary fraction. Based on observations spread over only 10 days, Evans et al. (2006) reported a particularly low observed binary fraction of only $(4 \pm 2)\%$. In

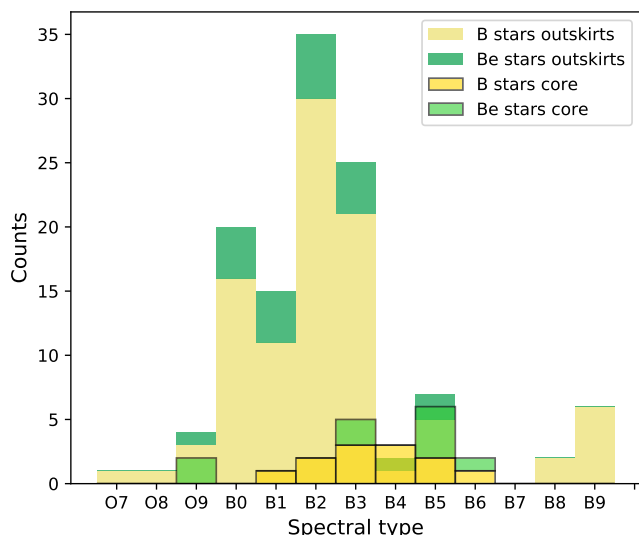


Fig. 18. Distribution of spectral types from Evans et al. (2006, outskirts) compared to the MUSE data (see Fig. 14) of the core. The sample of Evans et al. contains no stars fainter than $V = 17$, therefore we cut our sample at this brightness to facilitate the comparison.

this study, based on a single epoch, we find a lower limit on the observed binary fraction of $(14 \pm 2)\%$, which is higher than the fraction derived by Evans et al. (2006).

These findings combined reveal that the stellar contents of the core and the outskirts are clearly different: the stars in the outskirts are significantly younger. We note that this is the opposite of what was found in 30 Doradus, where the core cluster (R136) is significantly younger than the average age of the massive stars in NGC 2070 and the wider region (Crowther et al. 2016; Schneider et al. 2018).

The two distinct populations seen in and around NGC 330 could be explained by different star-formation histories, with the older cluster contrasting with younger stars formed as part of the ongoing (more continuous) star formation in the SMC bar. When we consider the 35–40 Myr age of the cluster, feedback from the time at which the most massive stars in the cluster exploded as supernovae could have helped instigate star formation in the outskirts.

Alternatively, rejuvenated runaway or walkway stars (see, e.g., Renzo et al. 2019) could contribute to the younger population in the outskirts. These stars would be the mass gainers in previous binary interactions (thus appearing rejuvenated) that had been ejected when their previously more massive companions exploded as supernovae. Assuming a low ejection velocity of 5 km s^{-1} , a star would travel 50 pc within 10 Myr, which indicates that the population of the outskirts (i.e., outside the MUSE FoV) by runaway or walkway stars is possible.

A more detailed study is required to understand the formation history of these populations. It needs to be supported by detailed physical parameters of the stars and combined with dynamical information from their radial velocities and proper motions.

6. Summary and future work

This is a first study of the dense core of the SMC cluster NGC 330 using the MUSE-WFM equipped with the new AO. The unprecedented spatial resolution of MUSE WFM-AO allows us to spectroscopically study the massive star population in the dense core of the cluster for the first time. We automati-

cally extracted and normalized spectra for more than 250 stars. We find that a vast majority of them are B-type stars, but there are also two Oe stars and a handful of RSGs and BSGs. About 30% of the B stars (and both O stars) show broad spectral lines characteristic of rapid rotation and emission features primarily in $H\alpha$, but also in other spectral lines like He I and O I. They are therefore classified as classical Be (Oe) stars. We derive a lower limit on the observed binary fraction of $14 \pm 2\%$.

Using archival HST data, we were able to position our stars in a CMD and investigated their evolutionary status. By comparison to single-star nonrotating Padova isochrones, we estimate a cluster age between 35 and 40 Myr and a total cluster mass of $M_{\text{tot,NGC330}} = 88_{-18}^{+17} \times 10^3 M_{\odot}$. This mass can be used to compare our findings for NGC 330 to clusters of similar masses but different ages, for example, RSGC 01, RSGC 02, RSGC 03, or NGC 6611 in the Milky Way, and NGC 1818, NGC 1847, or NGC 2100 in the LMC (Portegies Zwart et al. 2010).

We find several stars that are hotter and brighter than the MS turnoff, indicative of blue straggler stars, which are thought to be binary-interaction products. Two of these stars, classified as Oe/Be stars, are the stars of earliest spectral type in our sample and could have been spun up to high rotational velocities in previous binary interactions.

By comparison of our findings to the spectroscopic study of 120 OB stars in the outskirts of NGC 330 by Evans et al. (2006), we find significant differences in the spectral type distribution, the Be star fraction, and the binary fraction. We conclude that the stellar content of the core is significantly different from the content in the outskirts and discuss possible explanations.

In subsequent papers of this series, we will determine the current multiplicity fraction of all stars in the sample using the six available epochs. This will also allow us to characterize the variability of the Be stars in the sample. Subsequently, we will combine all six epochs to increase the S/N of the data, which will allow us to model the stars in order to derive their effective temperatures, surface gravities, rotation rates, and abundances for the brightest stars. This will allow us to further investigate the BiP candidates we identified in this paper and characterize the star formation history of NGC 330.

Acknowledgements. J.B. acknowledges support from the FWO_Odysseus program under project G0F8H6N. L.R.P. acknowledges support from grant AYA2015-68012-C2-1-P from the Spanish Ministry of Economy and Competitiveness (MINECO). SdM acknowledges funding by the European Union’s Horizon 2020 research and innovation programme from the European Research Council (ERC) (Grant agreement No. 715063), and by the Netherlands Organisation for Scientific Research (NWO) as part of the Vidi research program BinWaves with project number 639.042.728. This research has made use of the SIMBAD database, operated at CDS, Strasbourg, France and of NASA’s Astrophysics Data System Bibliographic Services. Parts of the analysis in this project are based on the python code PHOTUTILS. We are grateful to the staff of the ESO Paranal Observatory for their technical support.

References

- Ahumada, J. A., & Lapasset, E. 2007, *A&A*, **463**, 789
 Alecian, E., Neiner, C., Wade, G. A., et al. 2015, in *Proc. International Astronomical Union*, eds. G. Meynet, C. Georgy, J. Groh, & P. Stee, 307, 330
 Anderson, J., & King, I. R. 2000, *PASP*, **112**, 1360
 Aoki, W., Tominaga, N., Beers, T. C., Honda, S., & Lee, Y. S. 2014, *Science*, **345**, 912
 Arp, B. H. 1959, *AJ*, **64**, 254
 Bacon, R., Accardo, M., Adjali, L., et al. 2010, in *Ground-based and Airborne Instrumentation for Astronomy III*, eds. I. S. McLean, S. K. Ramsay, & H. Takami, *Proc. SPIE*, **7735**, 773508
 Bartolini, C., Dapergol, A., & Piccioni, A. 1981, *Inf. Bull. Variab. Stars*, **2010**, 1

- Bastian, N., Cabrera-Ziri, I., Niederhofer, F., et al. 2017, *MNRAS*, **465**, 4795
- Beasor, E. R., Davies, B., Smith, N., & Bastian, N. 2019, *MNRAS*, **486**, 266
- Bischoff, R., Mugrauer, M., Zehe, T., et al. 2017, *Astron. Nachr.*, **338**, 671
- Blaauw, A. 1993, in *Massive Stars: Their Lives in the Interstellar Medium*, eds. J. Cassinelli, & E. B. Churchwell, *ASP Conf. Ser.*, **35**, 207
- Bodenheimer, P. 1995, *ARA&A*, **33**, 199
- Bodensteiner, J., Baade, D., Greiner, J., & Langer, N. 2018, *A&A*, **618**, A110
- Böhm, T., Lignières, F., Wade, G., et al. 2012, *A&A*, **537**, A90
- Bouw, G. D. 1981, *PASP*, **93**, 45
- Bradley, L., Sipocz, B., Robitaille, T., et al. 2019, <https://doi.org/10.5281/zenodo.2533376>
- Bragança, G. A., Daflon, S., Cunha, K., et al. 2012, *AJ*, **144**, 130
- Bresolin, F., Crowther, P. A., & Puls, J. 2008, in *Massive Stars as Cosmic Engines* (Cambridge: Cambridge University Press), *Proc. IAU*, 250
- Bressan, A., Marigo, P., Girardi, L., et al. 2012, *MNRAS*, **427**, 127
- Britavskiy, N., Lennon, D. J., Patrick, L. R., et al. 2019, *A&A*, **624**, A128
- Bromm, V., Yoshida, N., Hernquist, L., & McKee, C. F. 2009, *Nature*, **459**, 49
- Brott, I., Evans, C. J., Hunter, I., et al. 2011, *A&A*, **530**, A116
- Carney, B. W., Janes, K. A., & Flower, P. J. 1985, *AJ*, **90**, 1196
- Chalabaev, A., & Maillard, J. P. 1983, *A&A*, **127**, 279
- Chen, Y., Girardi, L., Bressan, A., et al. 2014, *MNRAS*, **444**, 2525
- Chen, Y., Bressan, A., Girardi, L., et al. 2015, *MNRAS*, **452**, 1068
- Clark, J. S., Ritchie, B. W., Najarro, F., Langer, N., & Negueruela, I. 2014, *A&A*, **565**, A90
- Conti, P. S., & Alschuler, W. R. 1971, *ApJ*, **170**, 325
- Cowley, A., Cowley, C., Jaschek, M., & Jaschek, C. 1969, *AJ*, **74**, 375
- Crowther, P. A., Caballero-Nieves, S. M., Bostroem, K. A., et al. 2016, *MNRAS*, **458**, 624
- de Mink, S. E., Pols, O. R., & Hilditch, R. W. 2007, *A&A*, **467**, 1181
- de Mink, S. E., Langer, N., Izzard, R. G., Sana, H., & de Koter, A. 2013, *ApJ*, **764**, 166
- de Mink, S. E., Sana, H., Langer, N., Izzard, R. G., & Schneider, F. R. N. 2014, *ApJ*, **782**, 7
- de Rossi, M. E., Tissera, P. B., & Pedrosa, S. E. 2010, *A&A*, **519**, A89
- Deb, S., & Singh, H. P. 2010, *MNRAS*, **402**, 691
- Donati, J. F., Howarth, I. D., Jardine, M. M., et al. 2006, *MNRAS*, **370**, 629
- Dorda, R., Negueruela, I., González-Fernández, C., & Marco, A. 2018, *A&A*, **618**, A137
- Dunstall, P. R., Dufton, P. L., Sana, H., et al. 2015, *A&A*, **580**, A93
- Ekström, S., Meynet, G., Maeder, A., & Barblan, F. 2008, *A&A*, **478**, 467
- Evans, C. J., Lennon, D. J., Smartt, S. J., & Trundle, C. 2006, *A&A*, **456**, 623
- Evans, C. J., Taylor, W. D., Hénault-Brunet, V., et al. 2011, *A&A*, **530**, A108
- Feast, M. W. 1972, *MNRAS*, **159**, 113
- Feast, M. W., & Black, C. 1980, *MNRAS*, **191**, 285
- Ferraro, F. R., Paltrinieri, B., Fusi Pecci, F., et al. 1997, *A&A*, **324**, 915
- Gaia Collaboration (Brown, A. G. A., et al.) 2018, *A&A*, **616**, A1
- Gies, D. R., Bagnuolo, Jr., W. G., Ferrara, E. C., et al. 1998, *ApJ*, **493**, 440
- Gies, D. R., & Bolton, C. T. 1986, *ApJS*, **61**, 419
- Gies, D. R., Mason, B. D., Hartkopf, W. I., et al. 1993, *AJ*, **106**, 2072
- Gordon, K. D., Clayton, G. C., Misselt, K. A., Landolt, A. U., & Wolff, M. J. 2003, *ApJ*, **594**, 279
- Gosnell, N. M., Mathieu, R. D., Geller, A. M., et al. 2014, *ApJ*, **783**, L8
- Gray, R. O., & Corbally, C. J. 1994, *AJ*, **107**, 742
- Gray, R. O., & Corbally, C. J. 2009, *Stellar Spectral Classification* (Princeton: Princeton University Press)
- Gray, R. O., & Garrison, R. F. 1987, *ApJS*, **65**, 581
- Gray, R. O., Corbally, C. J., Garrison, R. F., McFadden, M. T., & Robinson, P. E. 2003, *AJ*, **126**, 2048
- Grebel, E. K., Richter, T., & de Boer, K. S. 1992, *A&A*, **254**, L5
- Grebel, E. K., Roberts, W. J., & Brandner, W. 1996, *A&A*, **311**, 470
- Greiner, S., Baylac, M.-O., Rolland, L., et al. 1999, *A&AS*, **137**, 451
- Haberl, F., & Sturm, R. 2016, *A&A*, **586**, A81
- Hanuschik, R. W., Kozok, J. R., & Kaiser, D. 1988, *A&A*, **189**, 147
- Harries, T. J., Hilditch, R. W., & Howarth, I. D. 2003, *MNRAS*, **339**, 157
- Hilditch, R. W., Howarth, I. D., & Harries, T. J. 2005, *MNRAS*, **357**, 304
- Hoogerwerf, R., de Bruijne, J. H. J., & de Zeeuw, P. T. 2001, *A&A*, **365**, 49
- Jamet, L., Perez, E., Cervino, M., et al. 2004, *A&A*, **426**, 399
- Kaufer, A., Stahl, O., Tubbesing, S., et al. 1999, *The Messenger*, **95**, 8
- Keller, S. C., & Bessell, M. S. 1998, *A&A*, **340**, 397
- Keller, S. C., Wood, P. R., & Bessell, M. S. 1999, *AS*, **134**, 489
- Kerton, C. R., Ballantyne, D. R., & Martin, P. G. 1999, *AJ*, **117**, 2485
- Kobulnicky, H. A., Lundquist, M. J., Bhattacharjee, A., & Kerton, C. R. 2012, *AJ*, **143**, 71
- Kobulnicky, H. A., Kiminki, D. C., Lundquist, M. J., et al. 2014, *ApJS*, **213**, 34
- Kochanek, C. S., Auchettl, K., & Belczynski, K. 2019, *MNRAS*, **485**, 5394
- Kroupa, P. 2001, *MNRAS*, **322**, 231
- Langer, N. 2012, *ARA&A*, **50**, 107
- Lennon, D. J., Mazzali, P. A., Pasian, F., Bonifacio, P., & Castellani, V. 1993, *Space Sci. Rev.*, **66**, 169
- Levato, O. H. 1972, *PASP*, **84**, 584
- Lobel, A. A., Achmad, L., de Jager, C., & Nieuwenhuijzen, H. 1992, *A&A*, **256**, 159
- Mackey, A. D., & Gilmore, G. F. 2002, *MNRAS*, **338**, 120
- Maeder, A., Grebel, E. K., & Mermilliod, J.-C. 1999, *A&A*, **346**, 459
- Mahy, L., Nazé, Y., Rauw, G., et al. 2009, *A&A*, **502**, 937
- Mahy, L., Sana, H., Abdul-Masih, M., et al. 2020, *A&A*, in press, <https://doi.org/10.1051/0004-6361/201936151>
- Marigo, P., Girardi, L., Bressan, A., et al. 2017, *ApJ*, **835**, 77
- Martayan, C., Floquet, M., Hubert, A.-M., et al. 2007a, *A&A*, **472**, 577
- Martayan, C., Frémat, Y., Hubert, A.-M., et al. 2007b, *A&A*, **462**, 683
- Martayan, C., Baade, D., & Fabregat, J. 2010, *A&A*, **509**, A11
- Mazzali, P., Lennon, D., Pasian, F., et al. 1996, *A&A*, **316**, 173
- McLaughlin, D. E., & van der Marel, R. P. 2005, *ApJS*, **161**, 304
- McLeod, A. F., Dale, J. E., Evans, C., et al. 2019, *MNRAS*, **486**, 5263
- Milone, A. P., Marino, A. F., Di Criscienzo, M., et al. 2018, *MNRAS*, **477**, 2640
- Morgan, W. W., & Keenan, P. C. 1973, *ARA&A*, **11**, 29
- Packet, W. 1981, *A&A*, **102**, 17
- Pastorelli, G., Marigo, P., Girardi, L., et al. 2019, *MNRAS*, **485**, 5666
- Patrick, L. R., Lennon, D. J., Evans, C. J., et al. 2020, *A&A*, in press, <https://doi.org/10.1051/0004-6361/201936741>
- Podsiadlowski, P., Joss, P. C., & Hsu, J. J. L. 1992, *ApJ*, **391**, 246
- Pols, O., Cote, J., Waters, L. B. F. M., & Heise, J. 1991, *A&A*, **241**, 419
- Portegies Zwart, S. F., McMillan, S. L. W., & Gieles, M. 2010, *ARA&A*, **48**, 431
- Ramírez-Agudelo, O. H., Simón-Díaz, S., Sana, H., et al. 2013, *A&A*, **560**, A29
- Ramírez-Agudelo, O. H., Sana, H., de Mink, S. E., et al. 2015, *A&A*, **580**, A92
- Ramírez-Tannus, M. C., Cox, N. L. J., Kaper, L., & de Koter, A. 2018, *A&A*, **620**, A52
- Raskin, G., Van Winckel, H., Hensberge, H., et al. 2011, *A&A*, **526**, A69
- Reig, P. 2011, *Ap&SS*, **332**, 1
- Renzo, M., Zapartas, E., de Mink, S. E., et al. 2019, *A&A*, **624**, A66
- Rivinius, T., Carciofi, A. C., & Martayan, C. 2013, *A&ARv*, **21**, 69
- Robertson, J. W. 1974, *A&AS*, **15**, 261
- Rodríguez, E., de Lopez Coca, P., & Rolland, A. 1991, *Inf. Bull. Variab. Stars*, **3625**, 1
- Sana, H., & Evans, C. J. 2011, *IAU Symp.*, **6**, 474
- Sana, H., de Koter, A., de Mink, S. E., et al. 2013, *A&A*, **550**, A107
- Sana, H., de Mink, S. E., de Koter, A., et al. 2012, *Science*, **337**, 444
- Sandage, A. R. 1953, *AJ*, **58**, 61
- Schaerer, D., Meynet, G., Maeder, A., & Schaller, G. 1993, *A&AS*, **98**, 523
- Schild, R. E., & Chaffee, F. 1971, *ApJ*, **169**, 529
- Schneider, F. R. N., Izzard, R. G., de Mink, S. E., et al. 2014, *ApJ*, **780**, 117
- Schneider, F. R. N., Izzard, R. G., Langer, N., & de Mink, S. E. 2015, *ApJ*, **805**, 20
- Schneider, F. R. N., Podsiadlowski, P., Langer, N., Castro, N., & Fossati, L. 2016, *MNRAS*, **457**, 2355
- Schneider, F. R. N., Ramírez-Agudelo, O. H., Tramper, F., et al. 2018, *A&A*, **618**, A73
- Shara, M. M., Saffer, R. A., & Livio, M. 1997, *ApJ*, **489**, L59
- Shtykovskiy, P., & Gilfanov, M. 2005, *MNRAS*, **362**, 879
- Sirianni, M., Nota, A., De Marchi, G., Leitherer, C., & Clampin, M. 2002, *ApJ*, **579**, 275
- Sota, A., Apellániz, J. M., Morrell, N. I., et al. 2014, *ApJS*, **211**, 10
- Sota, A., Maíz Apellániz, J., Walborn, N. R., et al. 2011, *ApJS*, **193**, 24
- Stetson, P. B. 1987, *PASP*, **99**, 191
- Sturm, R., Haberl, F., Pietsch, W., et al. 2013, *A&A*, **558**, A3
- Szewczuk, W., & Daszyńska-Daszkiewicz, J. 2015, *MNRAS*, **453**, 277
- Taam, R. E., & Sandquist, E. L. 2000, *ARA&A*, **38**, 113
- Tang, J., Bressan, A., Rosenfield, P., et al. 2014, *MNRAS*, **445**, 4287
- Telting, J. H., & Schrijvers, C. 1998, *A&A*, **339**, 150
- Townsend, R. H. D., Owocki, S. P., & Howarth, I. D. 2004, *MNRAS*, **350**, 189
- van Belle, G. T., & von Braun, K. 2009, *ApJ*, **694**, 1085
- Vanbeveren, D., & De Loore, C. 1994, *A&A*, **290**, 129
- Vanbeveren, D., & Mennekens, N. 2017, in *The B[e] Phenomenon: Forty Years of Studies*, eds. A. Miroshnichenko, S. Zharikov, D. Korčáková, & M. Wolf (San Francisco: ASP), 121
- Verbunt, F. 1993, *ARA&A*, **31**, 93
- Walborn, N. R. 1982, *AJ*, **87**, 1300
- Walborn, N. R., & Fitzpatrick, E. L. 1990, *PASP*, **102**, 379
- Wang, L., Gies, D. R., & Peters, G. J. 2017, *ApJ*, **843**, 60
- Wang, L., Gies, D. R., & Peters, G. J. 2018, *ApJ*, **853**, 156
- Zeidler, P., Sabbini, E., Nota, A., et al. 2018, *AJ*, **156**, 211
- Zorec, J., & Briot, D. 1997, *A&A*, **318**, 443
- Zorec, J., Frémat, Y., & Cidale, L. 2005, *A&A*, **441**, 235

Appendix A: Spectral extraction in crowded regions

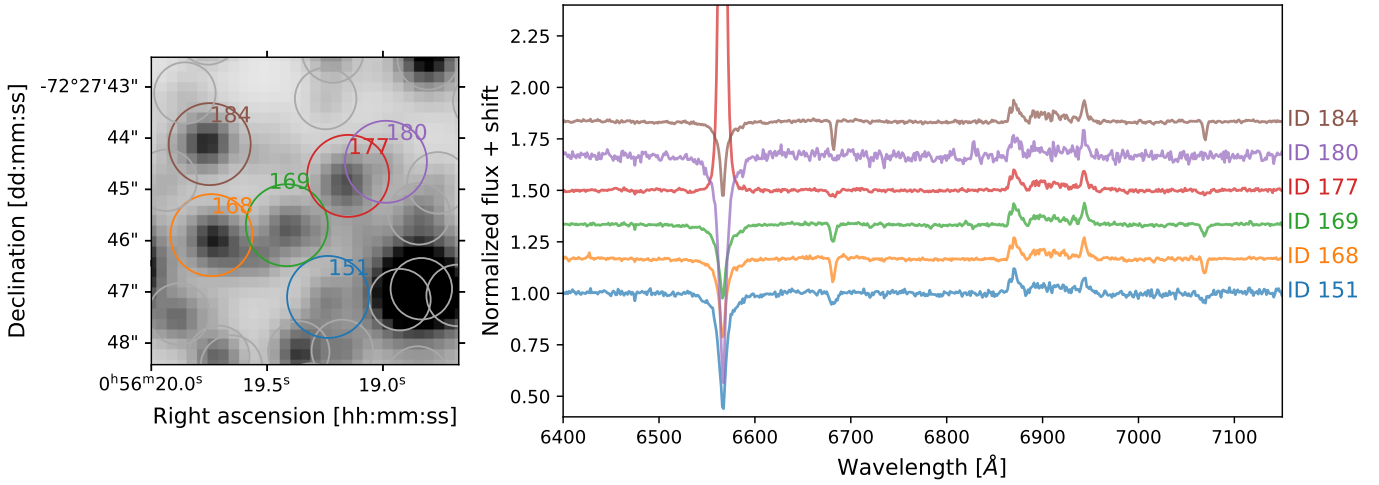


Fig. A.1. Example spectral extraction for star 459. All stars within a 12-pixel distance from the target star (marked with colored circles in the *left panel*) are taken into account in the extraction of the spectrum. The spectra of all considered stars are shown in the *right panel*. The spectrum of star 459 does not show signs of contamination by its surrounding stars.

The crowding of the observed field means that the extraction of spectra is difficult. We developed a spectral extraction routine based on the PYTHON package PHOTUTILS that is based on PSF extraction. For each star, we took all sources within a distance of 12 pixels (corresponding to $2.4''$) into account by simultaneously fitting their PSF. One example is shown in Fig. A.1, where the spectrum of star 459 is extracted.

Appendix B: Be star spectral classification

As described in Sect. 4.1, our automated spectral classification method reveals its limitations for Be stars because of the infilling of spectral lines by emission from the Be star disk. In addition to

the automatic classification, we therefore assigned spectral types to the Be stars by comparing their spectra to a set of standard star spectra by eye. We accounted for the possible rapid rotation of the Be stars by artificially broadening the standard star spectra to a rotational velocity of 200 km s^{-1} . Furthermore, we rebinned them to lower resolution to resemble the MUSE spectra. One example of this classification is shown in Fig. B.1. The star shown here is classified as a B5e star.

For a majority of the Be stars in our sample, the two methods agree within the errors. In cases of disagreement, we kept the spectral type derived by visual inspection because this method allows us to take more spectral lines into account.

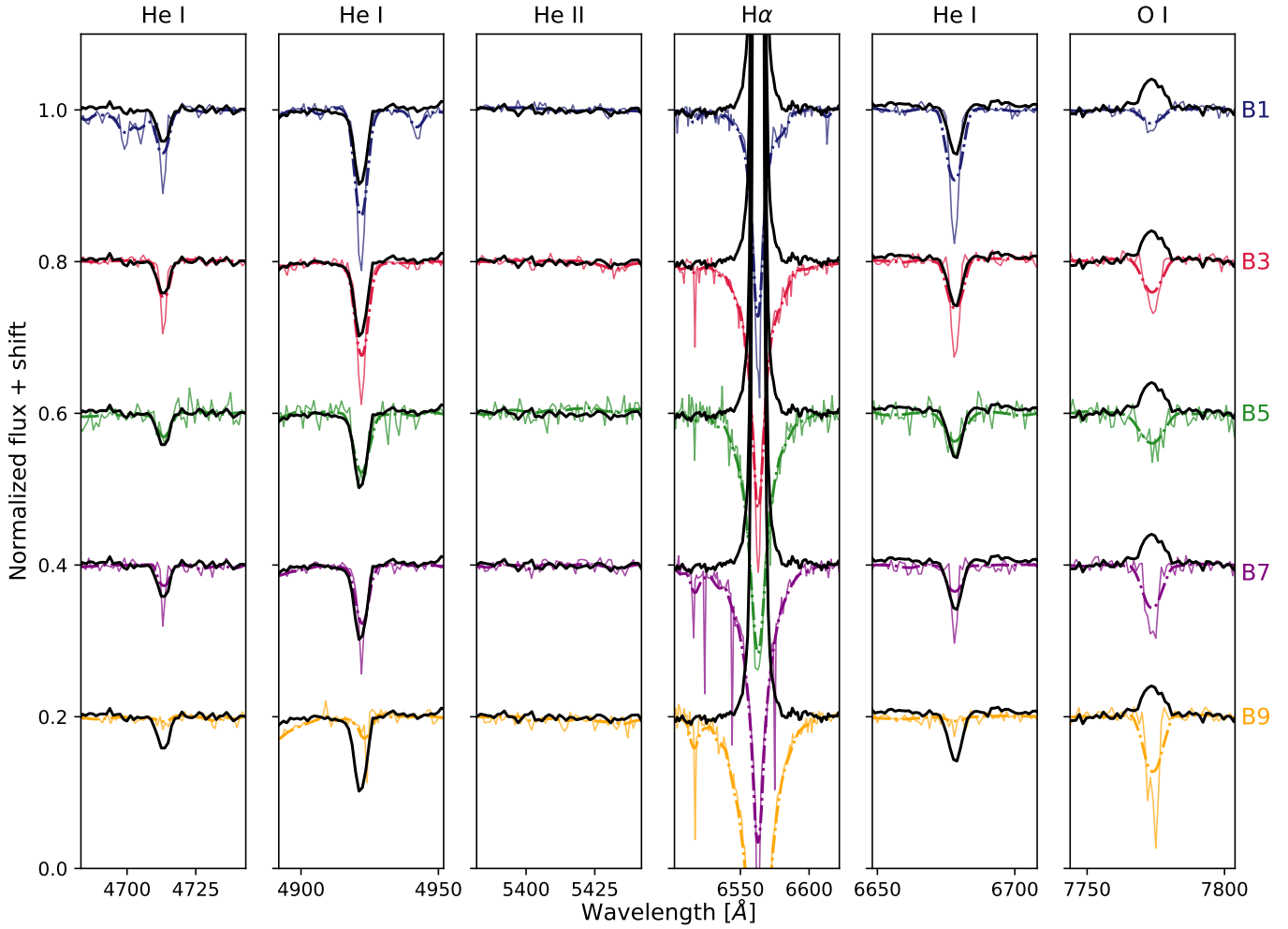


Fig. B.1. Example Be star spectral classification of star 290. The MUSE spectrum of the star that has to be classified is shown in black. Overplotted and shifted vertically for clarity are a set of standard star spectra (as described in Sect. 4.1) of spectral types B1 to B9, degraded to the MUSE resolution. While the continuous line shows the observed standard star spectrum, the dash-dotted line is rotationally broadened by 200 km s^{-1} .

Appendix C: Color magnitude diagram

As mentioned in Sect. 5.2, none of the isochrones reproduces the lower part of the MS, that is, mainly stars fainter than $F814W = 20 \text{ mag}$. While they reproduce the upper part of the MS well, the isochrones are systematically too faint by $\approx 0.3 \text{ mag}$ around the MS kink.

A shift to brighter magnitudes is equivalent to assuming a shorter distance to the cluster (i.e., a distance of $\approx 48 \text{ kpc}$). Because of the distance to the SMC and hence the distance to NGC 330, we refrain from varying the distance.

Varying the extinction toward the SMC does not remove this discrepancy either because the extinction affects the $F336W$ and $F814W$ filters differently and thus changes the shape of the isochrones on the CMD.

Appendix D: Tables with equivalent width measurements

Table D.1 gives an overview over the coordinates, V -band magnitudes, the measured EW with errors for all B-type stars, spectral types, and possible comments.

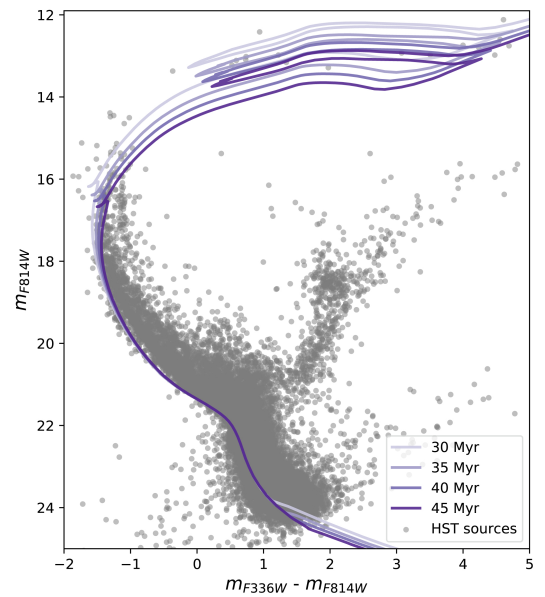


Fig. C.1. Zoomed-out version of Fig. 16 including stars fainter than $F814W = 20 \text{ mag}$. None of the isochrones reproduces the lower part of the MS.

Table D.1. Compilation of all parameters derived for the sample stars.

Identifier BSM #	RA [J2000]	Dec [J2000]	V [mag]	EW_{5412} [Å]	EW_{6678} [Å]	EW_{7774} [Å]	Class	SpType	Comments
001	14.053752	-72.472051	18.28	0.057 ± 0.074	0.573 ± 0.070	-0.138 ± 0.101	B	B4	–
002	14.071623	-72.471556	18.22	-0.018 ± 0.065	0.351 ± 0.068	0.008 ± 0.085	B	B6	–
003	14.093478	-72.470921	17.53	–	–	–	Be	B5e	–
004	14.065192	-72.470558	18.26	0.049 ± 0.055	0.295 ± 0.078	-0.053 ± 0.084	B	B6	–
...									
042	14.07937325	-72.46877809	13.50	–	–	–	RSG	K1 Ib	Arp II-18
...									

Notes. The first, second, and third columns give the identifier as well as coordinates. The column “ V ” gives the apparent V magnitude (derived as described in Sect. 3.1). We then give an overview over the measured EWs, EW errors, and derived spectral types for all B-type stars. For Be stars, we give the spectral type derived with the by-eye method. For the RSGs and BSGs, we include the information shown already in Table 2. The last column lists comments. A full version of this table is available at the CDS. The first few lines are shown as an example.